Journal of Sound and Vibration 330 (2011) 245–270

Contents lists available at ScienceDirect

Journal of Sound and Vibration

journal homepage: www.elsevier.com/locate/jsvi

Voids at the tunnel–soil interface for calculation of ground vibration from underground railways

Simon Jones *, Hugh Hunt

Department of Engineering, Cambridge University, Cambridge CB2 1PZ, UK

ARTICLE INFO

Article history:
Received 24 September 2009
Received in revised form
2 August 2010
Accepted 9 August 2010
Handling Editor: M.P. Cartmell
Available online 21 August 2010

ABSTRACT

Voids at the tunnel–soil interface are not normally considered when predicting ground vibration from underground railways. The soil is generally assumed to be continuously bonded to the outer surface of the tunnel to simplify the modelling process. Evidence of voids around underground railways motivated the study presented herein to quantify the level of uncertainty in ground vibration predictions associated with neglecting to include such voids at the tunnel–soil interface. A semi-analytical method is developed which derives discrete transfers for the coupled tunnel–soil model based on the continuous Pipe-in-Pipe method. The void is simulated by uncoupling the appropriate nodes at the interface to prevent force transfer between the systems. The results from this investigation show that relatively small voids ($4\,\text{m} \times 90^{\circ}$) can significantly affect the rms velocity predictions in the near-field and moderately affect predictions in the far-field. Sensitivity of the predictions to void length and void sector angle are both deemed to be significant. The findings from this study suggest that the uncertainty associated with assuming a perfect bond at the tunnel–soil interface in an area with known voidage can reasonably reach ± 5 dB and thus should be considered in the design process.

1. Introduction

Underground railways in urban centers are an efficient and economic means of mass transport. Urban rail systems are increasingly promoted as developments in tunneling, rail and train technologies allow old lines to be upgraded and new lines to be constructed under existing city infrastructure. Ground-borne vibration from these underground railways can impair human comfort and activity, damage buildings, or cause malfunctioning of sensitive equipment [1,2]. It is reported that individuals experience greater levels of disturbance due to rail noise [3] than from aircraft or road traffic [4–7]. This is attributed to the multiple ways people experience railway induced vibrations: air-borne noise, vibratory motion of the floors, and re-radiated noise both in the room and from household objects.

The frequency range of interest is between 5 and 200 Hz as listed in BS 6472:1992 [1] and BS ISO 14837–1[8]. Higher frequencies are generally attenuated rapidly with distance along the transmission path through the soil [9]; lower frequencies are weakly excited and generally below the threshold of human perception [10,11]. The vibrations of interest arise principally from the quasi-static load of the train moving along the track [12], general wheel and rail unevenness, and periodic changes in rail-support stiffness when sleepers are present [13]. The draft standard BS ISO 14837-2 quantifies acceptable vibration levels from new underground railways.

* Corresponding author. Tel.: +44 7846 012592.
E-mail address: sj335@cam.ac.uk (S. Jones).

0022-460X/$ - see front matter © 2010 Elsevier Ltd. All rights reserved.
doi:10.1016/j.jsv.2010.08.015

Designers of underground railways and surrounding buildings rely on vibration predictions from numerical simulations to ensure that vibration does not exceed specified levels; failure to meet the specifications can result in costly retrofitting of vibration countermeasures. A number of different numerical methods are currently used to predict ground vibration due to underground railways where semi-analytical methods, finite-element (FE) methods and boundary-element (BE) methods are the most common. Both two-dimensional [14,15] and three-dimensional [16–18] models based on FE and BE techniques have been developed but each suffers from its own set of difficulties. Andersen and Jones [19] compare coupled FE–BE models in 2D and 3D showing that while 2D models require less computation effort they prove to be only qualitatively useful when simulating structural changes. Three-dimensional models provide quantitative results but require significantly more computational effort than 2D models.

To combine the benefits of 2D and 3D models, Sheng et al. [20–22] simulate a tunnel buried in a half-space using a coupled FE–BE model derived using the discrete wavenumber fictitious force method. The boundary integral equation is written solely in terms of the displacement Green's function, proving to be more computationally efficient than standard boundary-element techniques which also require a traction Green's function. The method assumes the model geometry is invariant in the tunnel's axial direction which simplifies the model into a "two-and-a-half" dimensional problem. Degrande et al. [23,24] use the homogeneity along the tunnel in a slightly different manner. The periodicity of the tunnel and the soil is exploited using the Floquet transform, limiting the discretization to a single bounded reference cell of the tunnel modelled using the coupled FE–BE method. The authors state that this is a major advantage compared to the standard 2.5D approach because the use of periodic cells rather than 2D slices allows any type of loading, including point forces, to be more easily simulated. Gupta et al. have used this method in a number of published studies including the prediction of vibrations due to underground railways in Beijing [25] and the investigation of tunnel and soil parameters on ground vibration [26]. Forrest and Hunt [13,27,28] present a computationally efficient, three-dimensional semi-analytical model for calculating vibration from underground railways, known as Pipe-in-Pipe (PiP). A cylindrical tunnel and surrounding soil are modelled as two concentric pipes; the inner-pipe (i.e. the tunnel) is modelled using thin-shell theory and the outer-pipe (i.e. the soil) is modelled using elastic continuum theory and assumed to have an infinite outer radius simulating a fullspace. The PiP model has been validated against the FE–BE–Floquet model [29] and shown to have good agreement. Hussein and Hunt [30–32] have since extended the model to include discontinuous floating-slab track, soil layering and a free-surface. However, none of these models have been used to investigate the importance of voids at the tunnel–soil interface.

A simplifying assumption frequently made is that the soil is in continuous contact with the tunnel (i.e. no voids or gaps at the tunnel–soil interface). Subsidence and frost-heave have been shown to cause significant soil movement around tunnels [33–35]; under such large-scale motion it is likely that a void will form over a section of the tunnel, disrupting the perfect bond at the tunnel–soil interface. Voids may also develop during construction of new buildings in close proximity to the underground tunnels due to pile-driving, excavation, landscaping, etc. The extent of voidage is difficult, if not impossible, to quantify but the existence of voids is not in doubt.

The goal of the current investigation is to quantify the effect of voids at the tunnel–soil interface and determine the level of uncertainty associated with neglecting to include voids in numerical simulations of underground railways. Development of a fully analytical model including a finite sized void arbitrarily located around the tunnel was deemed intractable thus a semi-analytical approach is adopted. The PiP method is used to determine the discrete transfer functions for both the tunnel and the surrounding soil nodes. The transfer matrices are coupled using continuity and equilibrium conditions. The void is simulated by uncoupling the appropriate tunnel and soil nodes, inhibiting the transfer of forces between the two subsystems over a finite patch.

The current paper is broken into three sections. Section 2 presents the model and details how a void at the tunnel–soil interface is simulated; the theory of random-process moving loads is also introduced in this section. Section 3 compares the results from the discrete formulation to the PiP solution for a continuous tunnel–soil interface to validate the model. Section 4 presents near- and far-field soil vibration results due to a moving load in a tunnel containing a void at the tunnel–soil interface.

2. Model description

An idealized underground railway tunnel can be thought of as a thin-walled cylinder (i.e. the tunnel) coupled to the inside surface of a thick-walled cylinder (i.e. the surrounding soil), as shown in Fig. 1. If the outer radius of the thick-walled cylinder is assumed to be infinite (R_2 in Fig. 1(right)), this Pipe-in-Pipe arrangement provides the analytical solution for a buried, circular tunnel in a fullspace.

Forrest [13] derives the governing equations of motion for an infinitely long, thin-walled cylinder subjected to a radially acting point-load as

$$\tilde{\mathbf{U}}_n = \tilde{\mathbf{H}}_{\text{tunnel}} \tilde{\mathbf{P}}_n \tag{1}$$

where $\tilde{\mathbf{U}}_n$ and $\tilde{\mathbf{P}}_n$ are the cylindrical displacement and load vectors, respectively, in the $\{Z\ \theta\ R\}^{\mathrm{T}}$ directions; $\tilde{\mathbf{H}}_{\text{tunnel}}$ is a 3×3 matrix whose elements are given in the Appendix. The capitalization of the variables indicates the frequency domain, the tilde indicates the wavenumber domain, while the subindex n refers to the corresponding ring-mode.

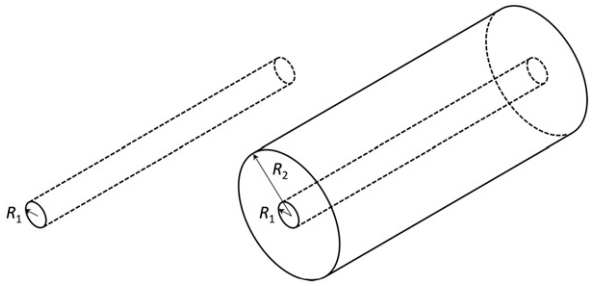

Fig. 1. Schematic of Pipe-in-Pipe arrangement: inner-pipe representing the tunnel modelled as a thin-walled cylinder (left) and outer-pipe representing the soil with outer radius $R_2=\infty$ (right).

Similarly, the governing equations of motion for an infinitely long, thick-walled cylinder subjected to a radially acting point-load is

$$\tilde{\mathbf{U}}_n = \tilde{\mathbf{H}}_{\text{soil}}\tilde{\mathbf{P}}_n \tag{2}$$

where the elements of $\tilde{\mathbf{H}}_{\text{soil}}$ are also given in the Appendix.

Coupling the two cylinders results in the development of reaction forces at the interface; the coupling equations of motion are

$$\tilde{\mathbf{U}}_n^{\text{tunnel}} = \tilde{\mathbf{H}}_{\text{tunnel}}\tilde{\mathbf{F}}_n + \tilde{\mathbf{H}}_{\text{tunnel}}\tilde{\mathbf{R}}_n^{\text{tunnel}} \tag{3}$$

$$\tilde{\mathbf{U}}_n^{\text{soil}} = \tilde{\mathbf{H}}_{\text{soil}}\tilde{\mathbf{R}}_n^{\text{soil}} \tag{4}$$

where $\tilde{\mathbf{F}}_n$ is the load applied to the inside of the tunnel and $\tilde{\mathbf{R}}_n$ is the resultant load between the tunnel and the soil at the cylindrical interface. Continuity of displacements and equilibrium of reaction forces at the interface state

$$\tilde{\mathbf{U}}_n^{\text{tunnel}} = \tilde{\mathbf{U}}_n^{\text{soil}} \equiv \tilde{\mathbf{U}}_n \tag{5}$$

$$\tilde{\mathbf{R}}_n^{\text{tunnel}} = -\tilde{\mathbf{R}}_n^{\text{soil}} \tag{6}$$

thus the coupled equations of motion for the system can be written as

$$\tilde{\mathbf{U}}_n = (\mathbf{I}+\tilde{\mathbf{H}}_{\text{tunnel}}\tilde{\mathbf{H}}_{\text{soil}}^{-1})^{-1}\tilde{\mathbf{H}}_{\text{tunnel}}\tilde{\mathbf{F}}_n \tag{7}$$

It is convenient to recognize that $\tilde{\mathbf{H}}_{\text{tunnel}}\tilde{\mathbf{F}}_n$ is equivalent to the displacements of the unconstrained tunnel (i.e. before being coupled to the soil). Let this displacement be referred to as the "original" displacement allowing the equation to be written as

$$\tilde{\mathbf{U}}_n = (\mathbf{I}+\tilde{\mathbf{H}}_{\text{tunnel}}\tilde{\mathbf{H}}_{\text{soil}}^{-1})^{-1}\tilde{\mathbf{U}}_n^{\text{orig}} \tag{8}$$

This form of the displacement equation is equivalent to that given by Forrest [13]; it is presented in this altered form for use in extending the model to account for voids.

The actual displacements and loads are in general linear combinations of an infinite number of ring-modes. For a radially acting point-load, the displacements are symmetric about the load with the axial and radial displacements even functions of θ and the circumferential displacements an odd function of θ. The displacement and load vectors can therefore be written as

$$\begin{Bmatrix} \tilde{U}_Z \\ \tilde{U}_\theta \\ \tilde{U}_R \end{Bmatrix} = \begin{Bmatrix} \tilde{U}_{Z_0} \\ 0 \\ \tilde{U}_{R_0} \end{Bmatrix} + \sum_{n=1}^{\infty} \begin{Bmatrix} \tilde{U}_{Zn}\cos\ n\theta \\ \tilde{U}_{\theta n}\sin\ n\theta \\ \tilde{U}_{Rn}\cos\ n\theta \end{Bmatrix} \tag{9}$$

$$\begin{gathered} \tilde{F}_{Zn} = 0 \\ \tilde{F}_{\theta n} = 0 \\ \tilde{F}_{Rn} = \begin{cases} 1/2\pi a, & n=0 \\ 1/\pi a, & n\geq 1 \end{cases} \end{gathered} \tag{10}$$

where θ is the radial angle coordinate measured from the location of the point-load. Eq. (9) is also valid for an axially acting point-load since $\tilde{U}_Z$ and $\tilde{U}_R$ are again even functions of θ about the point-load and $\tilde{U}_\theta$ is an odd function of θ. Hussein [30]

shows that for a circumferentially acting point-load the conditions switch, thus

$$\begin{Bmatrix} \tilde{U}_Z \\ \tilde{U}_\theta \\ \tilde{U}_R \end{Bmatrix} = \begin{Bmatrix} 0 \\ \tilde{U}_{\theta_0} \\ 0 \end{Bmatrix} + \sum_{n=1}^{\infty} \begin{Bmatrix} \tilde{U}_{Zn}\sin\ n\theta \\ \tilde{U}_{\theta n}\cos\ n\theta \\ \tilde{U}_{Rn}\sin\ n\theta \end{Bmatrix} \tag{11}$$

and certain elements of the matrices $\tilde{\mathbf{H}}_{\text{tunnel}}$ and $\tilde{\mathbf{H}}_{\text{soil}}$ change sign as detailed in the Appendix. The magnitude of a point-load in the frequency/wavenumber/ring-mode domain for the axial and circumferential directions is equivalent to that given in Eq. (10) for the radial direction.

2.1. Inclusion of floating-slab track in PiP model

A popular method of installing railway track in underground railways is to use a floating-slab track (FST) system. Rather than employing traditional wooden sleepers and crushed stone ballast, the rails are fastened to a concrete slab which sits on the base of the tunnel invert. To reduce vibration transmission the rails are generally mounted on resilient rubber railpads and the slab on rubber or steel-spring slab bearings as depicted in Fig. 2.

Forrest and Hussein have extensively investigated the modelling of FST (both continuous and discontinuous) using the PiP method for non-moving and moving loads [27,28,13,32,31,30]. A simple, continuous FST subjected to a quasi-static moving load is included in the current investigation; the more complex systems could be included using the methods derived in the referenced literature.

A schematic of the continuous FST model is shown in Fig. 3 where it has been simplified to a 2D system; the two rails are assumed to receive identical vertical inputs thus they are combined to a single beam. The rail and slab are modelled as Euler–Bernoulli beams with mass per unit length m and bending stiffness EI. The railpads and slab bearings are modelled as continuous layers of elastic support with stiffness per unit length k and associated loss factor η; the resulting complex stiffness is given by $k^* = k(1+\mathrm{i}\eta)$. The slab-bearing is assumed to only be in contact with the tunnel along the bottom of the invert (i.e. equivalent to a line-load). The FST properties used herein are given in Table 1 which approximate UIC60 rails on a standard continuous slab as used by Hussein [32].

The transfer function for an Euler–Bernoulli beam is [36]

$$\tilde{H}_{\text{beam}}(\xi,\omega) = \frac{1}{(EI\xi^4 - m\omega^2)} \tag{12}$$

where m is the mass per unit length, E is the elastic modulus, I is the second moment of area, ω is the frequency and ξ is the wavenumber in the x-direction as defined in Fig. 3.

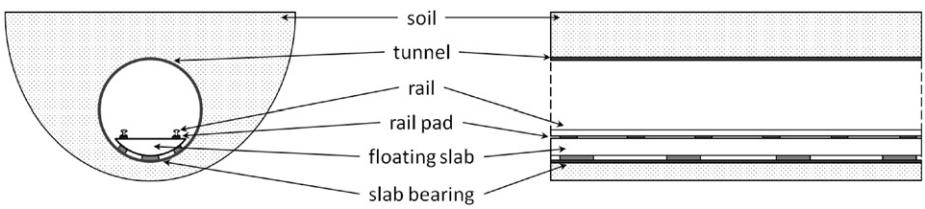

Fig. 2. Underground railway cut-away showing floating-slab track.

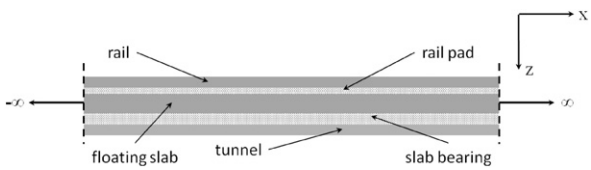

Fig. 3. Floating-slab track on tunnel invert.

Table 1
Floating-slab track properties.

Rail beam	**Slab beam**
m_{rail} = 120.6 kg/m	m_{slab} = 3500 kg/m
EI_{rail} = 12.9 MPa m^4	EI_{slab} = 1430 MPa m^4
Railpad	**Slab-bearing**
k_{rail} = 200 MN/m/m	k_{slab} = 5 MN/m/m
$\eta_{rail} = 0.3$	$\eta_{slab} = 0.5$

It is necessary to determine the transfer function for the FST assembly shown in Fig. 3 giving the displacements at the tunnel due to a load on the rail; this will be used to facilitate loading in the coupled tunnel–soil model. The transfer function is derived by enforcing displacement continuity and force equilibrium across the railpads and slab bearings resulting in

$$\begin{Bmatrix} \tilde{U}_{\text{rail}} \\ \tilde{U}_{\text{tunnel}} \end{Bmatrix} = \begin{Bmatrix} \tilde{H}_{rr} & \tilde{H}_{rt} \\ \tilde{H}_{tr} & \tilde{H}_{tt} \end{Bmatrix} \begin{Bmatrix} \tilde{F}_{\text{rail}} \\ \tilde{F}_{\text{tunnel}} \end{Bmatrix} \tag{13}$$

where

$$\begin{aligned}
\tilde{H}_{rr} &= \frac{\tilde{H}_{\text{tunnel}}(1+k^*_{\text{slab}}\tilde{H}_{\text{ss}})}{(1+k^*_{\text{slab}}\tilde{H}_{\text{ss}}+k^*_{\text{slab}}\tilde{H}_{\text{tunnel}})} \\
\tilde{H}_{rs} &= \frac{k^*_{\text{rail}}\tilde{H}_{\text{rail}}\tilde{H}_{\text{slab}}}{(1+k^*_{\text{rail}}\tilde{H}_{\text{slab}}+k^*_{\text{rail}}\tilde{H}_{\text{rail}})} = \tilde{H}_{sr} \\
\tilde{H}_{ss} &= \frac{\tilde{H}_{\text{slab}}(1+k^*_{\text{rail}}\tilde{H}_{\text{rail}})}{(1+k^*_{\text{rail}}\tilde{H}_{\text{slab}}+k^*_{\text{rail}}\tilde{H}_{\text{rail}})} \\
\tilde{H}_{rt} &= \frac{k^*_{\text{slab}}\tilde{H}_{\text{rs}}\tilde{H}_{\text{tunnel}}}{(1+k^*_{\text{slab}}\tilde{H}_{\text{ss}}+k^*_{\text{slab}}\tilde{H}_{\text{tunnel}})} = \tilde{H}_{tr} \\
\tilde{H}_{tt} &= \frac{\tilde{H}_{\text{ss}}(1+k^*_{\text{slab}}\tilde{H}_{\text{tunnel}})}{(1+k^*_{\text{slab}}\tilde{H}_{\text{ss}}+k^*_{\text{slab}}\tilde{H}_{\text{tunnel}})}
\end{aligned} \tag{14}$$

$\tilde{H}_{\text{tunnel}}$ is the *RR* component of $\tilde{\mathbf{H}}_{\text{tunnel}}$ as defined in Eq. (1).

Recall Eq. (8) which gives the coupled tunnel–soil interface displacements as a function of the original free-tunnel displacements

$$\tilde{\mathbf{U}}_n = (\mathbf{I}+\tilde{\mathbf{H}}_{\text{tunnel}}\tilde{\mathbf{H}}^{-1}_{\text{soil}})^{-1}\tilde{\mathbf{U}}^{\text{orig}}_n$$

Eq. (13) can be used to determine $\tilde{\mathbf{U}}^{\text{orig}}_n$ by setting $\tilde{F}_{\text{tunnel}} = 0$ giving

$$\tilde{\mathbf{U}}^{\text{orig}}_n = \tilde{H}_{tr}\tilde{F}^{\text{rail}}_n \tag{15}$$

If the load applied to the rail is assumed to be a point-load in the spatial domain, the load in the wavenumber domain is

$$\tilde{F}^{\text{rail}}_n = \begin{cases} 1/2\pi a, & n=0 \\ 1/\pi a, & n \geq 1 \end{cases} \tag{16}$$

as defined in Eq. (10).

It should be noted that $\tilde{\mathbf{H}}_{\text{tunnel}}$ in Eq. (8) is not adjusted to account for the presence of the FST when solving for the coupled tunnel–soil interface displacements. It was found the increased stiffness due to the FST was negligible compared to the concrete tunnel thus was neglected for simplicity.

During the derivation of the coupled tunnel–soil displacement equation it is assumed that the tunnel is in continuous contact with the soil, thus the PiP model in its standard form does not allow for discrete sections of the tunnel to be uncoupled from the soil. To investigate the effect of voids around the tunnel, the method is extended by discretizing the tunnel–soil interface.

2.2. Discrete tunnel–soil interface

To simulate voids using the PiP model the interface is discretized into a number of nodes with their respective transfer functions determined using the continuous solution. Once the global transfer function matrix for the interface is calculated, particular nodes can be uncoupled to simulate the void at the tunnel–soil interface.

Consider an example case shown in Fig. 4, where the circumference of the tunnel is discretized into eight nodes. A single unit point-load is applied in the positive radial direction at node 1, causing displacements at all nodes (displacements only depicted at nodes 1 and 3 for clarity). The nodal loading the *R*-direction can be written as

$$\tilde{\mathbf{F}}_R = [1\ \ 0\ \ 0\ \ 0\ \ 0\ \ 0\ \ 0\ \ 0]^{\text{T}} \tag{17}$$

The Fourier transform of this force is

$$\tilde{\mathbf{F}}_{Rn} = [1\ \ 1\ \ 1\ \ 1\ \ 1\ \ 1\ \ 1\ \ 1]^{\text{T}} \tag{18}$$

where the subscript n indicates the ring-mode domain; the discrete Fourier transform (DFT) is used to perform the transforms in this model.

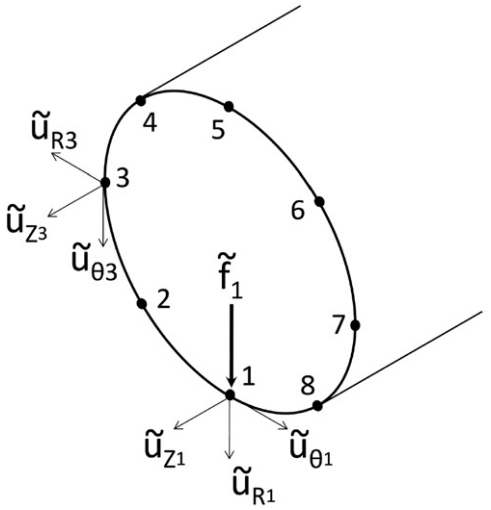

Fig. 4. Circumferential discretization of tunnel; example tunnel circumference discretized by eight nodes with a point-load applied radially at node 1, showing cylindrical coordinate directions.

The displacements in the ring-mode domain can be calculated for each term in the $\tilde{\mathbf{F}}_{Rn}$ vector using Eq. (1), resulting in

$$\begin{aligned}
\tilde{\mathbf{U}}_{ZRn} &= [\tilde{U}_{ZR_0}\ \tilde{U}_{ZR_1}\ \tilde{U}_{ZR_2}\ \tilde{U}_{ZR_3}\ \tilde{U}_{ZR_4}\ \tilde{U}_{ZR_5}\ \tilde{U}_{ZR_6}\ \tilde{U}_{ZR_7}]^{\mathrm{T}} \\
\tilde{\mathbf{U}}_{\theta Rn} &= [\tilde{U}_{\theta R_0}\ \tilde{U}_{\theta R_1}\ \tilde{U}_{\theta R_2}\ \tilde{U}_{\theta R_3}\ \tilde{U}_{\theta R_4}\ \tilde{U}_{\theta R_5}\ \tilde{U}_{\theta R_6}\ \tilde{U}_{\theta R_7}]^{\mathrm{T}} \\
\tilde{\mathbf{U}}_{RRn} &= [\tilde{U}_{RR_0}\ \tilde{U}_{RR_1}\ \tilde{U}_{RR_2}\ \tilde{U}_{RR_3}\ \tilde{U}_{RR_4}\ \tilde{U}_{RR_5}\ \tilde{U}_{RR_6}\ \tilde{U}_{RR_7}]^{\mathrm{T}}
\end{aligned} \tag{19}$$

Since the circumference of the cylinder is discretized into a finite number of points (N_{ring}), the Nyquist criterion restricts the largest ring-mode to $N_{\mathrm{ring}}/2$. Furthermore, Eq. (9) states that $\tilde{\mathbf{U}}_{ZRn}$ and $\tilde{\mathbf{U}}_{RRn}$ are even functions and $\tilde{\mathbf{U}}_{\theta Rn}$ is an odd function. Therefore the ring-mode coefficients are symmetric and anti-symmetric, respectively. The ring-mode coefficients are written in standard inverse DFT (IDFT) input notation as follows:

$$\begin{aligned}
\tilde{\mathbf{U}}_{ZRn} &= [\tilde{U}_{ZR_0}\ \tilde{U}_{ZR_1}\ \tilde{U}_{ZR_2}\ \tilde{U}_{ZR_3}\ \tilde{U}_{ZR_4}\ \tilde{U}_{ZR_3}\ \tilde{U}_{ZR_2}\ \tilde{U}_{ZR_1}]^{\mathrm{T}} \\
\tilde{\mathbf{U}}_{\theta Rn} &= [0\ -\mathrm{i}\tilde{U}_{\theta R_1}\ -\mathrm{i}\tilde{U}_{\theta R_2}\ -\mathrm{i}\tilde{U}_{\theta R_3}\ 0\ \mathrm{i}\tilde{U}_{\theta R_3}\ \mathrm{i}\tilde{U}_{\theta R_2}\ \mathrm{i}\tilde{U}_{\theta R_1}]^{\mathrm{T}} \\
\tilde{\mathbf{U}}_{RRn} &= [\tilde{U}_{RR_0}\ \tilde{U}_{RR_1}\ \tilde{U}_{RR_2}\ \tilde{U}_{RR_3}\ \tilde{U}_{RR_4}\ \tilde{U}_{RR_3}\ \tilde{U}_{RR_2}\ \tilde{U}_{RR_1}]^{\mathrm{T}}
\end{aligned} \tag{20}$$

Performing the IDFT results in a set of transfer function terms

$$\begin{aligned}
&\tilde{\mathbf{H}}_{Z_iR_1} \\
&\tilde{\mathbf{H}}_{\theta_iR_1} \\
&\tilde{\mathbf{H}}_{R_iR_1}
\end{aligned} \tag{21}$$

where each term represents the displacement (Z, θ, or R) of the ith node due to a radial point-load at node 1. This process is repeated to determine the transfer functions at every node due to loads acting in all three directions.

The transfer function terms can be arranged in matrix form as follows:

$$\begin{Bmatrix} \tilde{\mathbf{U}}_Z \\ \tilde{\mathbf{U}}_\theta \\ \tilde{\mathbf{U}}_R \end{Bmatrix} = \begin{bmatrix} \tilde{\mathbf{H}}_{Z_iZ_j} & \tilde{\mathbf{H}}_{Z_i\theta_j} & \tilde{\mathbf{H}}_{Z_iR_j} \\ \tilde{\mathbf{H}}_{\theta_iZ_j} & \tilde{\mathbf{H}}_{\theta_i\theta_j} & \tilde{\mathbf{H}}_{\theta_iR_j} \\ \tilde{\mathbf{H}}_{R_iZ_j} & \tilde{\mathbf{H}}_{R_i\theta_j} & \tilde{\mathbf{H}}_{R_iR_j} \end{bmatrix}_{\xi} \begin{Bmatrix} \tilde{\mathbf{F}}_Z \\ \tilde{\mathbf{F}}_\theta \\ \tilde{\mathbf{F}}_R \end{Bmatrix} = \tilde{\mathbf{H}}\tilde{\mathbf{F}} \tag{22}$$

which describes, for a given wavenumber ξ, the displacements at all nodes due to an arbitrary load applied with frequency ω. An IDFT is used to transform the set of transfer functions into the spatial domain, $\mathbf{H}_{\mathrm{tunnel}}$ and $\mathbf{H}_{\mathrm{soil}}$, thus the coupled equations of motion for the tunnel–soil system can be written in the spatial domain as

$$\mathbf{U} = (\mathbf{I} + \mathbf{H}_{\mathrm{tunnel}}\mathbf{H}_{\mathrm{soil}}^{-1})^{-1}\mathbf{U}^{\mathrm{orig}} \tag{23}$$

The wavenumber sampling and maximum values must be selected to ensure the discretization is sufficient to capture details at localized peaks as well as the far-field disturbance of travelling waves. The results from a convergence study investigating the effect of wavenumber properties on the response of a free-tunnel are shown in Fig. 5. The tunnel is

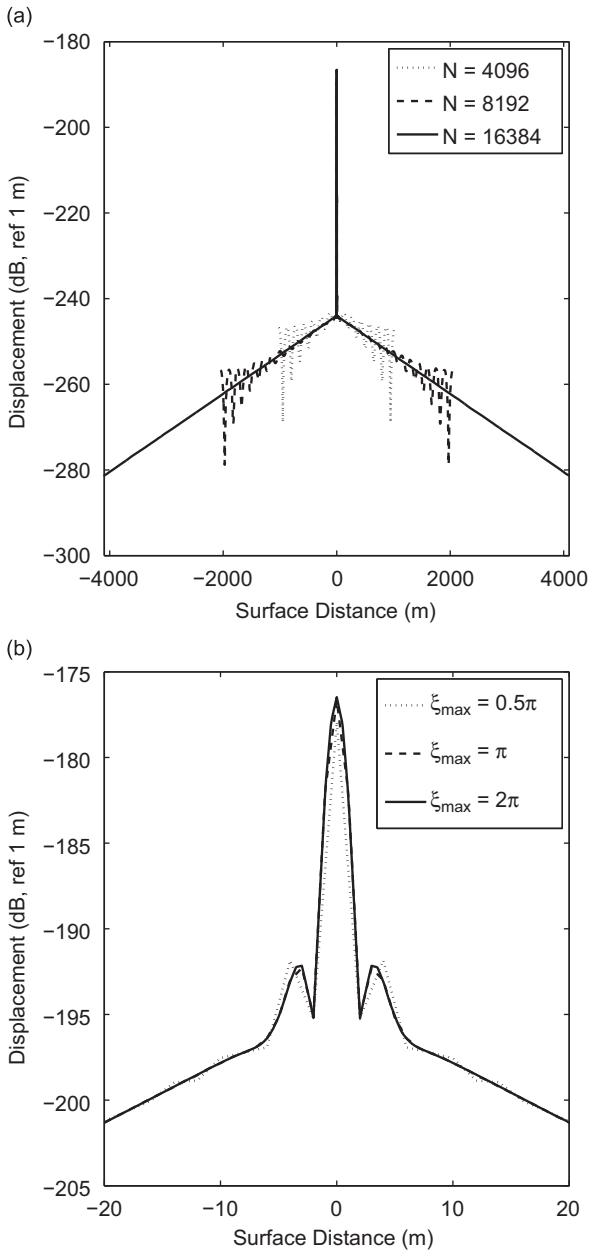

Fig. 5. Wavenumber parameter convergence testing for free-tunnel model subjected to a radial point-load at x=0.

subjected to a radially acting unit point-load at x=0 and the radial displacement response in the spatial domain along the base of the tunnel is plotted to determine convergence.

Fig. 5(a) shows the response at 15 Hz; at this low frequency the wavelengths are relatively long thus fine discretization in the wavenumber domain is required to capture the corresponding small wavenumbers. As the number of samples between $-2\pi < \xi < 2\pi$ is increased, the solution tends towards the converged solution at N=2^{14} samples. At higher frequencies the wavelengths are relatively short thus the maximum wavenumber must be increased to capture the localized peaks. Fig. 5(b) shows convergence of the solution at $\xi_{\max} = 2\pi$.

These wavenumber parameters (N=2^{14} and $\xi_{\max} = 2\pi$) were found to be sufficient to capture the response in the free-tunnel when the FST assembly is included and subjected to a point-load on the rail, as well as for the free-soil model subjected to a point-load. As such they are used throughout the remainder of the investigation. Note that these parameters result in a total model length of $-4096\,\mathrm{m} < x < 4096\,\mathrm{m}$ with $\Delta x = 0.5\,\mathrm{m}$.

This discretized spatial formulation of PiP allows nonuniform interaction between the tunnel and surrounding soil making it possible to simulate variable stiffness between the tunnel and soil, such as a void at the tunnel–soil interface.

2.3. Including a void in the discrete model

To simulate a void at the tunnel–soil interface, individual matching nodes on the tunnel and soil cylinders can be uncoupled. This allows the displacements of the two subsystems to differ at the void location while preventing any transfer of force between the tunnel and the soil. The degrees of freedom for both the tunnel and the soil are rearranged to group the coupled and uncoupled nodes:

$$\begin{Bmatrix} \mathbf{U}_c \\ \mathbf{U}_u \end{Bmatrix} = \begin{bmatrix} \mathbf{H}_{cc} & \mathbf{H}_{cu} \\ \mathbf{H}_{uc} & \mathbf{H}_{uu} \end{bmatrix} \begin{Bmatrix} \mathbf{F}_c \\ \mathbf{F}_u \end{Bmatrix} \tag{24}$$

where the subscripts c and u refer to the coupled and uncoupled degrees of freedom, respectively. Rewriting the continuity equations (Eqs. (3) and (4)) for the displacement of the coupled nodes gives

$$\mathbf{U}_{\mathrm{tunnel}_c} = \mathbf{H}_{\mathrm{tunnel}_{cc}}\mathbf{F}_c + \mathbf{H}_{\mathrm{tunnel}_{cu}}\mathbf{F}_u + \mathbf{H}_{\mathrm{tunnel}_{cc}}\mathbf{R}_{\mathrm{tunnel}_c} + \mathbf{H}_{\mathrm{tunnel}_{cu}}\mathbf{R}_{\mathrm{tunnel}_u} \tag{25}$$

$$\mathbf{U}_{\mathrm{soil}_c} = \mathbf{H}_{\mathrm{soil}_{cc}}\mathbf{R}_{\mathrm{soil}_c} + \mathbf{H}_{\mathrm{soil}_{cu}}\mathbf{R}_{\mathrm{soil}_u} \tag{26}$$

where displacement continuity and force equilibrium requires

$$\mathbf{U}_{\mathrm{tunnel}_c} = \mathbf{U}_{\mathrm{soil}_c} \tag{27a}$$

$$\mathbf{R}_{\mathrm{tunnel}_c} = -\mathbf{R}_{\mathrm{soil}_c} \tag{27b}$$

$$\mathbf{R}_{\mathrm{tunnel}_u} = -\mathbf{R}_{\mathrm{soil}_u} \tag{27c}$$

Assuming that no internal forces will be applied to the uncoupled nodes (i.e. $\mathbf{F}_u = \mathbf{0}$) and recalling that no resultant interface forces develop at these uncoupled nodes (i.e. $\mathbf{R}_u = \mathbf{0}$), Eqs. (25) and (26) can be combined as

$$\mathbf{U}_c = (\mathbf{I} + \mathbf{H}_{\mathrm{tunnel}_{cc}}\mathbf{H}^{-1}_{\mathrm{soil}_{cc}})^{-1}\mathbf{H}_{\mathrm{tunnel}_{cc}}\mathbf{F}_c \tag{28}$$

Noting that $\mathbf{H}_{\mathrm{tunnel}_{cc}}\mathbf{F}_c = \mathbf{U}_c^{\mathrm{orig}}$ Eq. (28) can be written as

$$\mathbf{U}_c = (\mathbf{I} + \mathbf{H}_{\mathrm{tunnel}_{cc}}\mathbf{H}^{-1}_{\mathrm{soil}_{cc}})^{-1}\mathbf{U}_c^{\mathrm{orig}} \tag{29}$$

which describes the displacement at the coupled degrees of freedom for the tunnel–soil model as a function of the original free-tunnel displacements at the coupled nodes. Eq. (29) is in a useful form to perform parametric studies of void parameters. $\mathbf{H}_{\mathrm{tunnel}}$ and $\mathbf{H}_{\mathrm{soil}}$ are the same for each case and need only be partitioned to include the appropriate nodes. $\mathbf{U}^{\mathrm{orig}}$ can be calculated relatively quickly and easily using the IDFT of Eq. (15); as $\mathbf{U}^{\mathrm{orig}}$ is only a function of the FST and tunnel parameters it is the same for all void cases. This allows for more efficient calculation when investigating numerous void parameters.

The resultant interface loads can be back-calculated from $\mathbf{U}_c$ using

$$\mathbf{H}^{-1}_{\mathrm{soil}_{cc}}\mathbf{U}_c = \mathbf{R}_c \tag{30}$$

and $\mathbf{R}_u = \mathbf{0}$. After rearranging the nodes back to the original order this resultant interface load vector can be used to determine the soil response at any desired radius R using

$$\mathbf{U}_R = \mathbf{H}_{\mathrm{soil}_R}\mathbf{R}_{\mathrm{interface}} \tag{31}$$

where $\mathbf{H}_{\mathrm{soil}_R}$ is derived in a similar way to the original soil transfer function at radius R. This formulation is also efficient for parametric studies of void parameters; $\mathbf{H}_{\mathrm{soil}_R}$ is the same for all void cases thus $\mathbf{U}_R$ can be calculated quickly for any case after the initial determination of the transfer function matrix.

This form of the solution can predict ground vibrations at any radius due to a dynamic load applied to the rail on the FST assembly at a fixed location. It is now useful to consider moving loads.

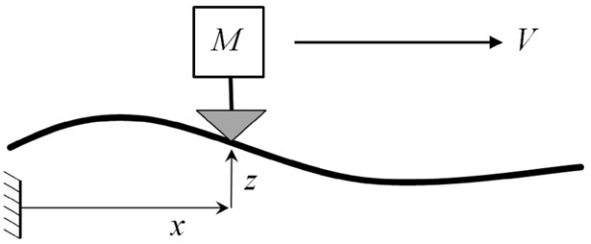

Fig. 6. Schematic of simple vehicle model.

2.4. Response due to a moving load

Amongst many others, Hussein and Hunt [31] show that a predominant loading mechanism on the tunnel invert is due to rail-roughness at the wheel–rail interface. For the purposes of the current investigation this loading mechanism is

Table 2
Third-octave passbands.

Reference name (Hz)	Passband (Hz)
20	17.8–22.4
25	22.4–28.2
31.5	28.2–35.5
40	35.5–44.7
50	44.7–56.2
63	56.2–70.8
80	70.8–89.1
100	89.1–112
125	112–141
160	141–178
200	178–224

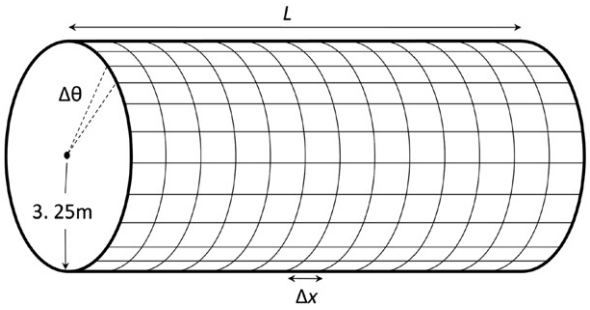

Fig. 7. Geometric parameters for model and mesh.

Table 3
Soil model properties.

	Tunnel	Soil
Elastic modulus (GPa)	$50(1+0.1i)$	$0.55(1+0.1i)$
Density (kg / m^3)	2500	2000
Poisson's ratio	0.3	0.44
P-wave speed (m/s)	5200	950
S-wave speed (m/s)	2800	310

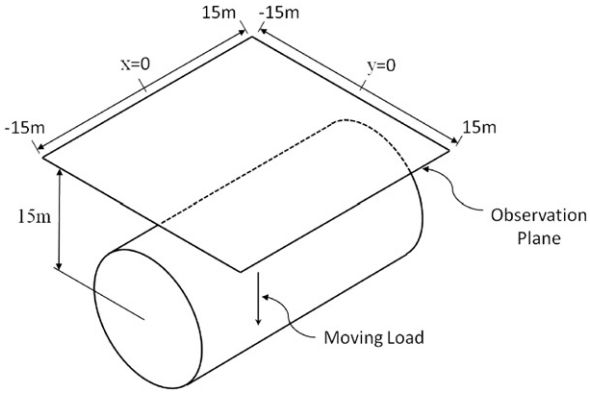

Fig. 8. Observation plane centered over the tunnel at height 15 m.

simplified to a single, moving point-load acting on the rail surface. The load is calculated using a single degree-of-freedom model of a 500 kg mass moving at constant speed along a rough rail (Fig. 6) as

$$F(x) = Ma(x) = -M\omega^2 z(x) \tag{32}$$

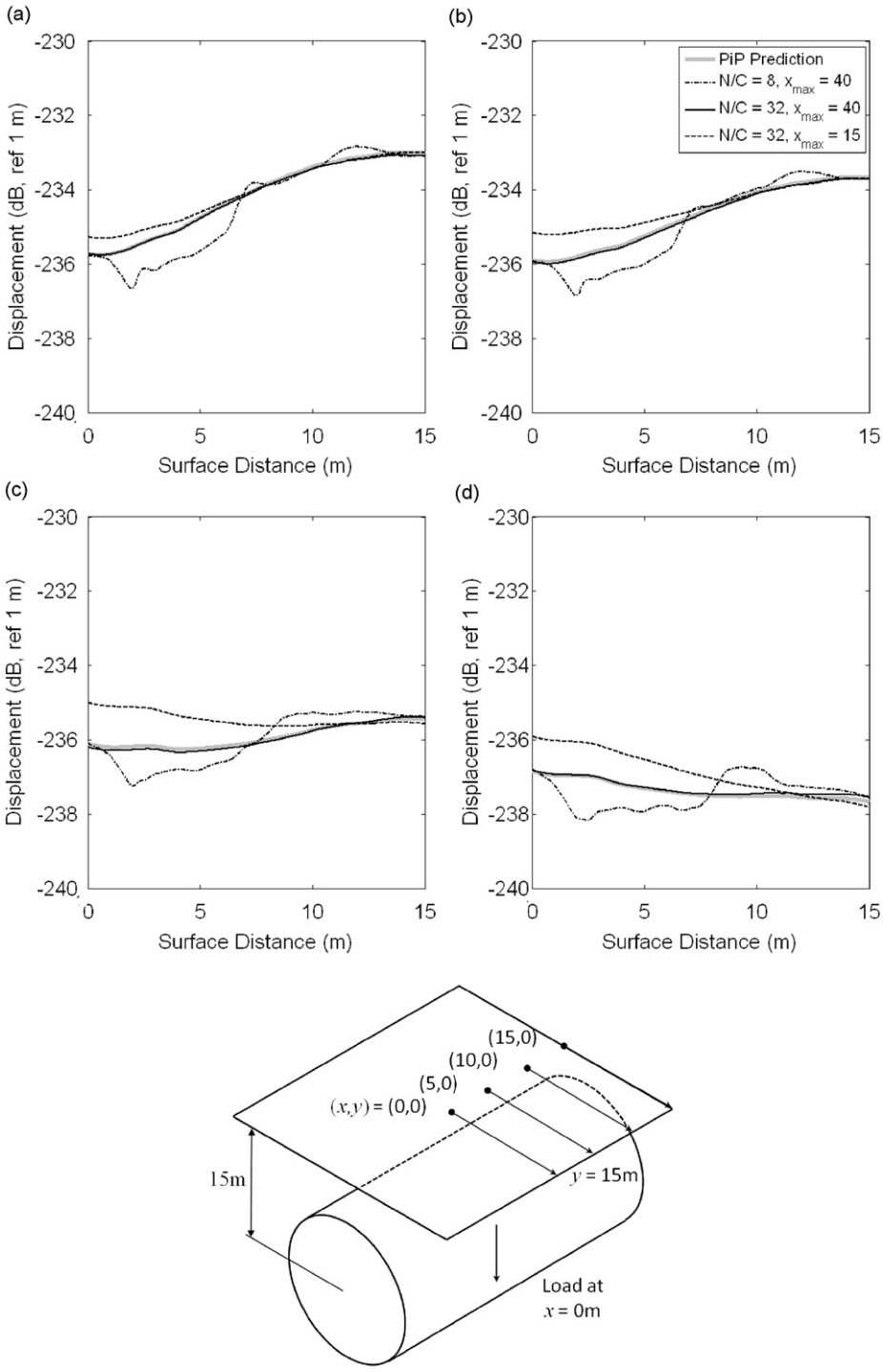

Fig. 9. Validation of discrete model against PiP at 15 Hz; three test cases shown for varying node density around the tunnel circumference (N/C) and axial length (x_{max}). (a) Origin (0,0), (b) origin (5,0), (c) origin (10,0) and (d) origin (15,0).

The rail-roughness profile is randomly distributed thus the theory of random vibrations [36] must be used to predict the resultant soil response. As the velocity of the moving load is much less than the shear-wave speed of the surrounding soil a quasi-stationary approximation of a non-stationary random vibration can be used [37]. This implies that the Doppler effect of the moving load is negligible so the load at any given point in time can be assumed a stationary random-process (i.e. the mean, mean square and standard deviation are all independent of time).

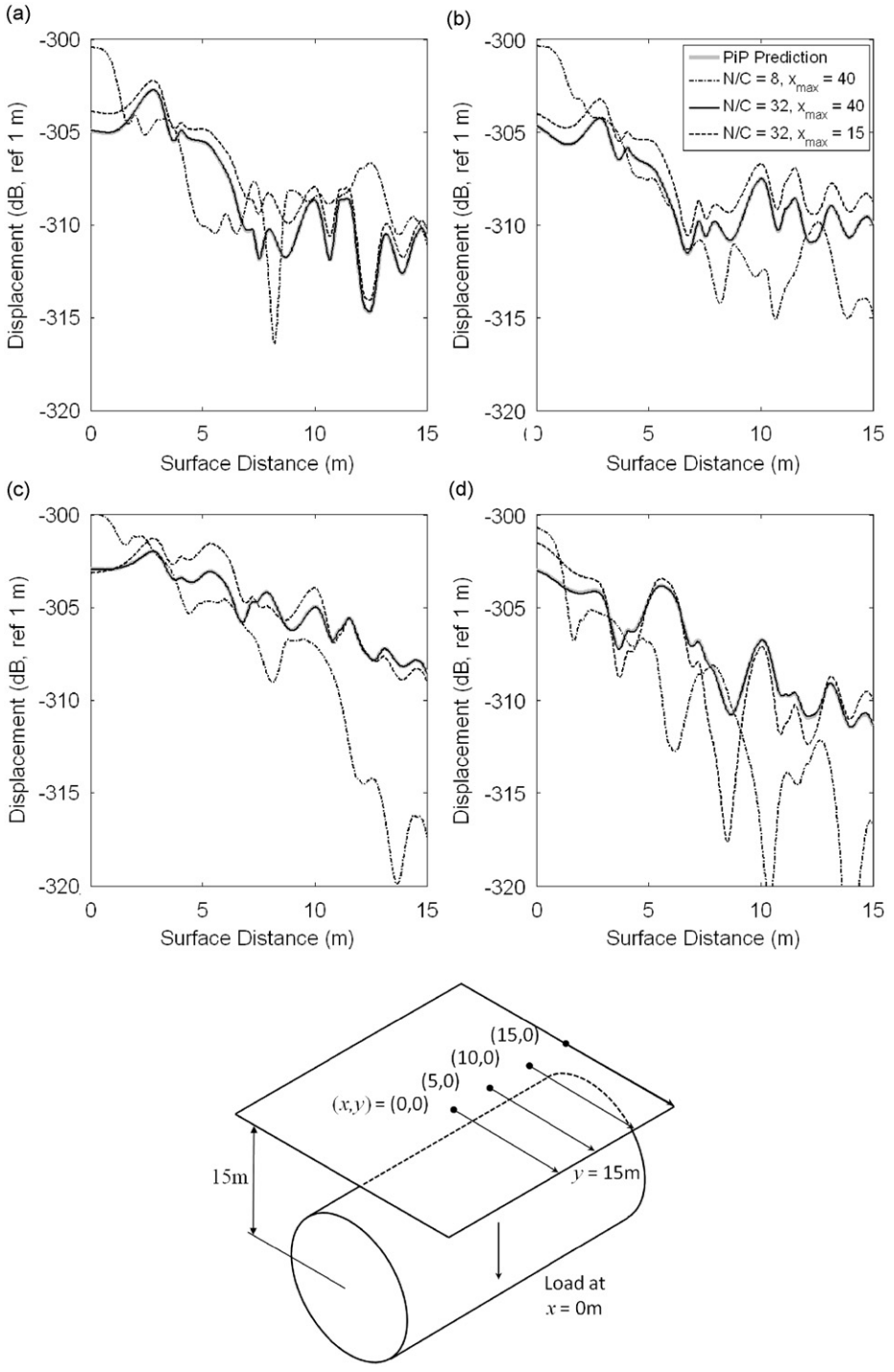

Fig. 10. Validation of discrete model against PiP at 200 Hz; three test cases shown for varying node density around the tunnel circumference (N/C) and axial length (x_{max}). (a) Origin (0,0), (b) origin (5,0), (c) origin (10,0) and (d) origin (15,0).

Frederich [38] provides an empirical formula for the single-sided rail-roughness spectrum based on track measurements. The average rail-roughness is calculated as follows:

$$S_\delta(\omega) = \frac{a}{v\left(b + \frac{\omega}{2\pi v}\right)^3} \tag{33}$$

where v is the load velocity (m/s), ω is the forcing frequency (rad/s), and a and b are constants describing the rail unevenness (1.31×10^{-2} mm^2/m^2 and 2.94×10^{-2}/m, respectively). Using Eq. (32) and standard random vibration theory [36], the force spectrum magnitude can be written as

$$S_f(\omega) = |m\omega^2|^2 S_\delta(\omega) \tag{34}$$

The discrete void model is used to determine the transfer function (H_{ij}) describing the displacement at an arbitrary point r_i in the surrounding soil for a point-load applied to the rail at x_j. The velocity spectrum magnitude at this arbitrary point is given by

$$S_v(\omega) = |(i\omega)H_{ij}|^2 S_f(\omega) \tag{35}$$

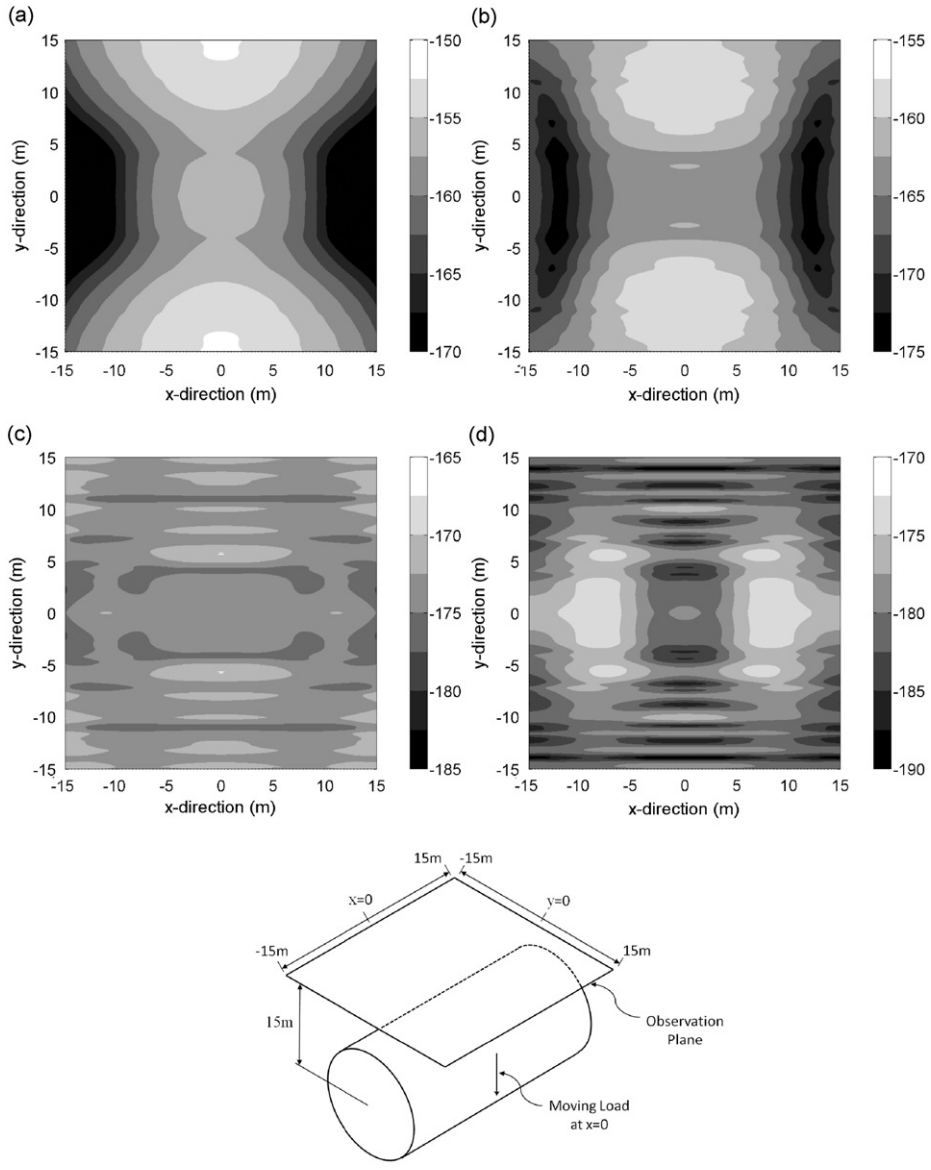

Fig. 11. Discrete model response for no void at (a) 25, (b) 50, (c) 100 and (d) 160 Hz third-octave passbands; response in rms velocity (dB, ref 1 m/s).

This velocity spectrum can be used to provide a measure of the mean-square velocity over a frequency band using the following property:

$$\mathrm{E}[v^2]_{\omega_1 \to \omega_2} = 2 \int_{\omega_1}^{\omega_2} S_v(\omega)\, \mathrm{d}\omega \tag{36}$$

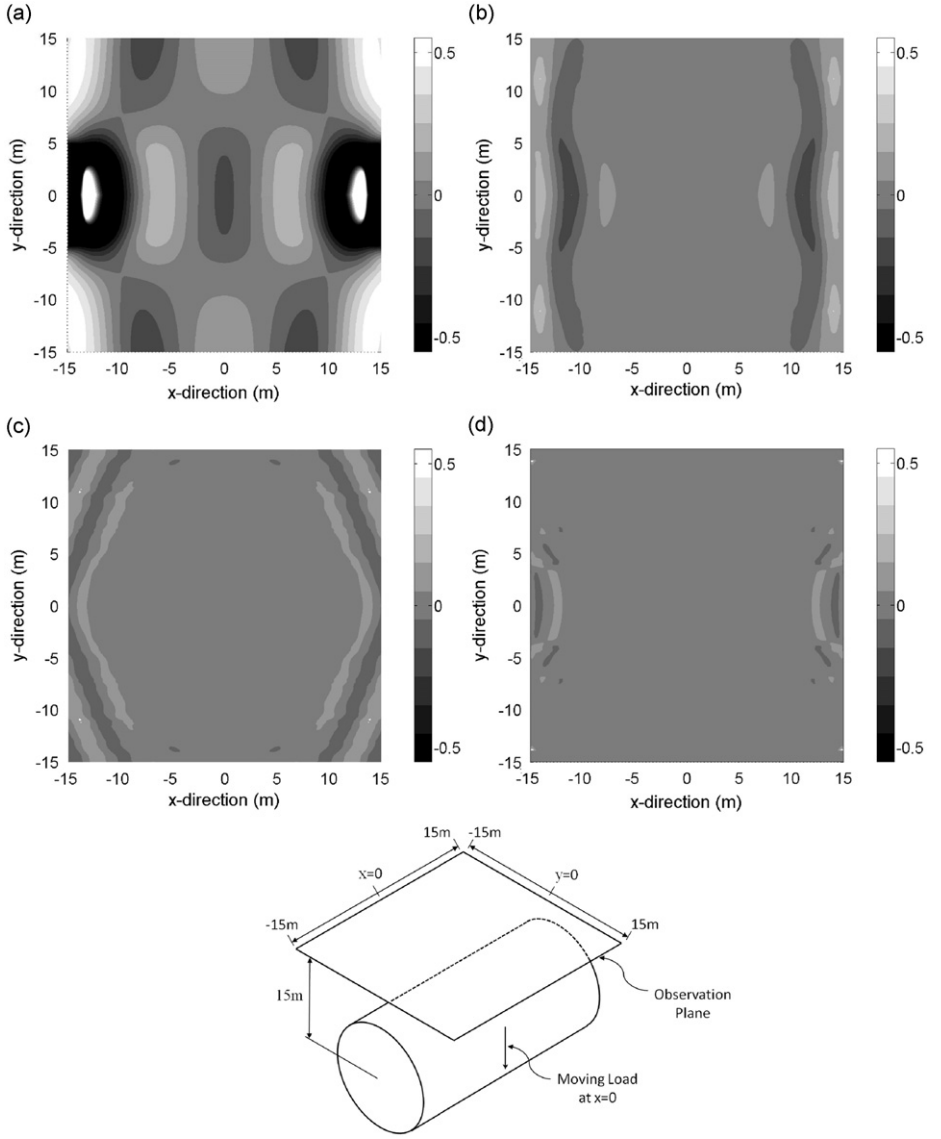

Fig. 12. Difference between discrete model and PiP response for no void at (a) 25, (b) 50, (c) 100 and (d) 160 Hz third-octave passbands; response in rms velocity (dB, ref 1 m/s).

Table 4
Void parameters—sensitivity to void length (VL) and void sector angle (VA).

Case	Void sector angle (deg)	Void length (m)
VL-1	67.5	2
VL-2	67.5	4
VL-3	67.5	6
VL-4	67.5	8
VA-1	45.0	4
VA-2	67.5	4
VA-3	90.0	4
VA-4	112.5	4

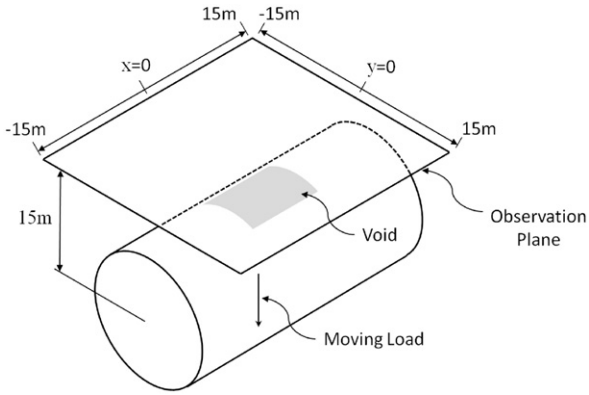

Fig. 13. Schematic showing void at tunnel–soil interface and observation plane centered over the tunnel at height 15 m.

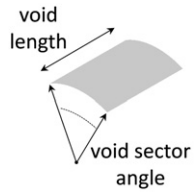

Fig. 14. Close-up schematic of the void showing the void parameters.

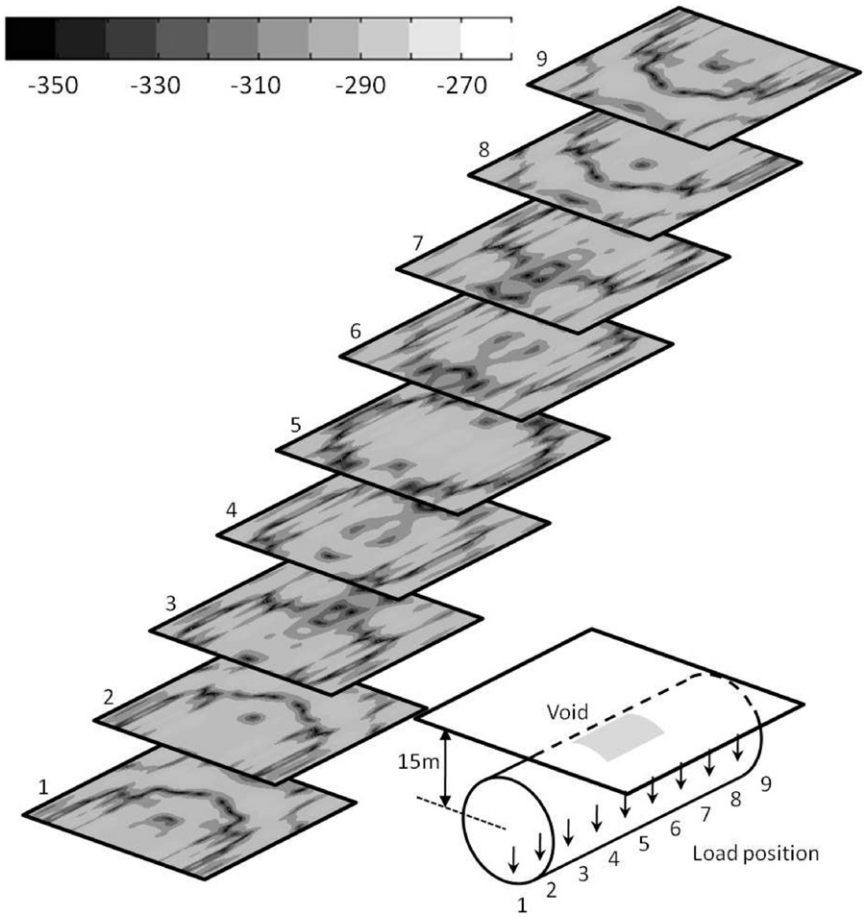

Fig. 15. Particle velocity response in dB (rms, ref 1 m/s) for case VA-3 at h=10 m as load moves along tunnel invert.

The rms velocity over the frequency band is simply the square-root of Eq. (36). Note this derivation of the $\omega_1 \rightarrow \omega_2$ passband rms velocity is equivalent to having a perfect passband filter which eliminates all input frequencies outside the band of interest. Although this is an idealized value it is still a useful measure of the vibration levels at different frequency passbands. The vertical rms velocities are determined in third-octave frequency bands according to Table 2.

The final step is to consider the slow variation of the rms particle velocity as the load travels along the length of the tunnel. This is best shown through the example detailed in Section 4. First it is sensible to validate the discrete model of a tunnel in continuous contact with the soil against PiP.

3. Validation of discrete model against PiP

A schematic of the 3D tunnel–soil interface used in the semi-analytical model is shown in Fig. 7; Table 3 lists the set of sample material properties used in the simulation of a 0.25 m thick concrete tunnel and surrounding soil. The vertical particle velocities are calculated for a 30 m × 30 m observation plane 15 m above the center of the tunnel as depicted in Fig. 8.

Recall that the free-tunnel and free-soil models were deemed to converge in the wavenumber domain for $N=2^{14}$ and $\xi_{max} = 2\pi$. This is equivalent to a total model length of $-4096\,\text{m} < x < 4096\,\text{m}$ with $\Delta x = 0.5\,\text{m}$. If, for example, 32 nodes are used around the circumference of the interface with three degrees of freedom each, this would result in a total of more than 1.5 million degrees of freedom; this is an impractical number of DOF's for a model which is intended for parametric studies with short computational times. When the tunnel is coupled to the soil model the system damping is greatly increased due to geometric decay and material damping in the soil. The hypothesis is that much less of the model in the axial direction will be required as the travelling waves will quickly decay.

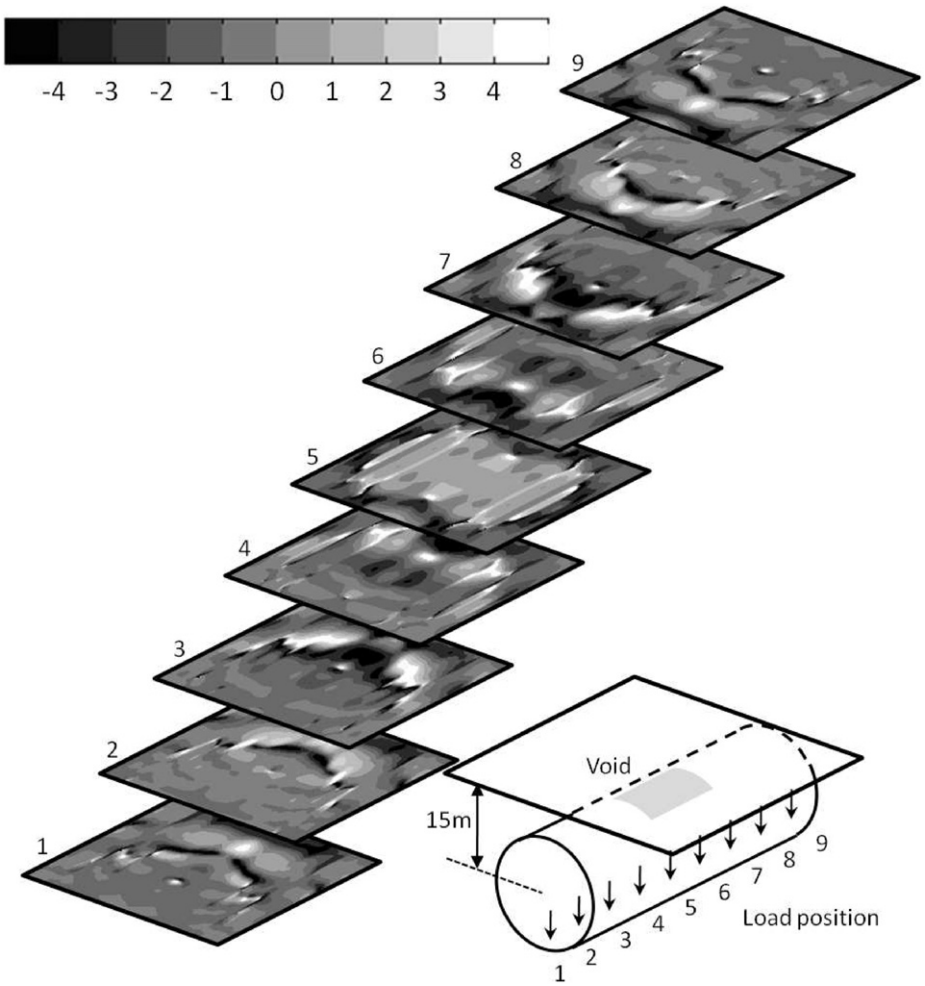

Fig. 16. Insertion gain response in dB (rms, ref 1 m/s) for case VA-3 at h=15 m as load moves along the tunnel invert.

To test this hypothesis a convergence test is performed to ensure that the spatial parameters of the tunnel–soil interface are sufficient to adequately represent the continuous bond at this interface. A harmonic load is applied to the rail at $x=0$ at 15 and 200 Hz (i.e. the limits of the frequency range of interest) and the displacement response is calculated along four horizontal lines 15 m above the tunnel extending perpendicular to the tunnel axis as depicted in Figs. 9 and 10. The effect of circumferential nodal density (nodes/circumference or N/C) and the half length of the model ($x_{\max}$) are illustrated in figures. Three representative sets of parameters are shown in comparison to the continuous PiP solution. The results are deemed to converge when refining the parameters results in less than a 1 percent relative difference at any x-location from the previous case; convergence was found to occur using 32 nodes per circumference with $x_{\max}$ = 40 m. As shown in Figs. 9 and 10 these model parameters result in predictions which agree well with the continuous PiP solution at the given locations and frequencies. The maximum difference between the two model predictions is 0.1 dB which occurs at $y=15$ m and 15 Hz (Fig. 9(d)).

The vertical rms particle velocities over the observation plane are predicted by the void-free discrete model using $N/C=32$ and x_{max} = 40 m. The results for the 25, 50, 100 and 160 Hz third-octave passbands are shown in Fig. 11 as a representative sample of the results; results are plotted in dB (rms, ref 1 m/s) when the moving load is at $x=0$. These results

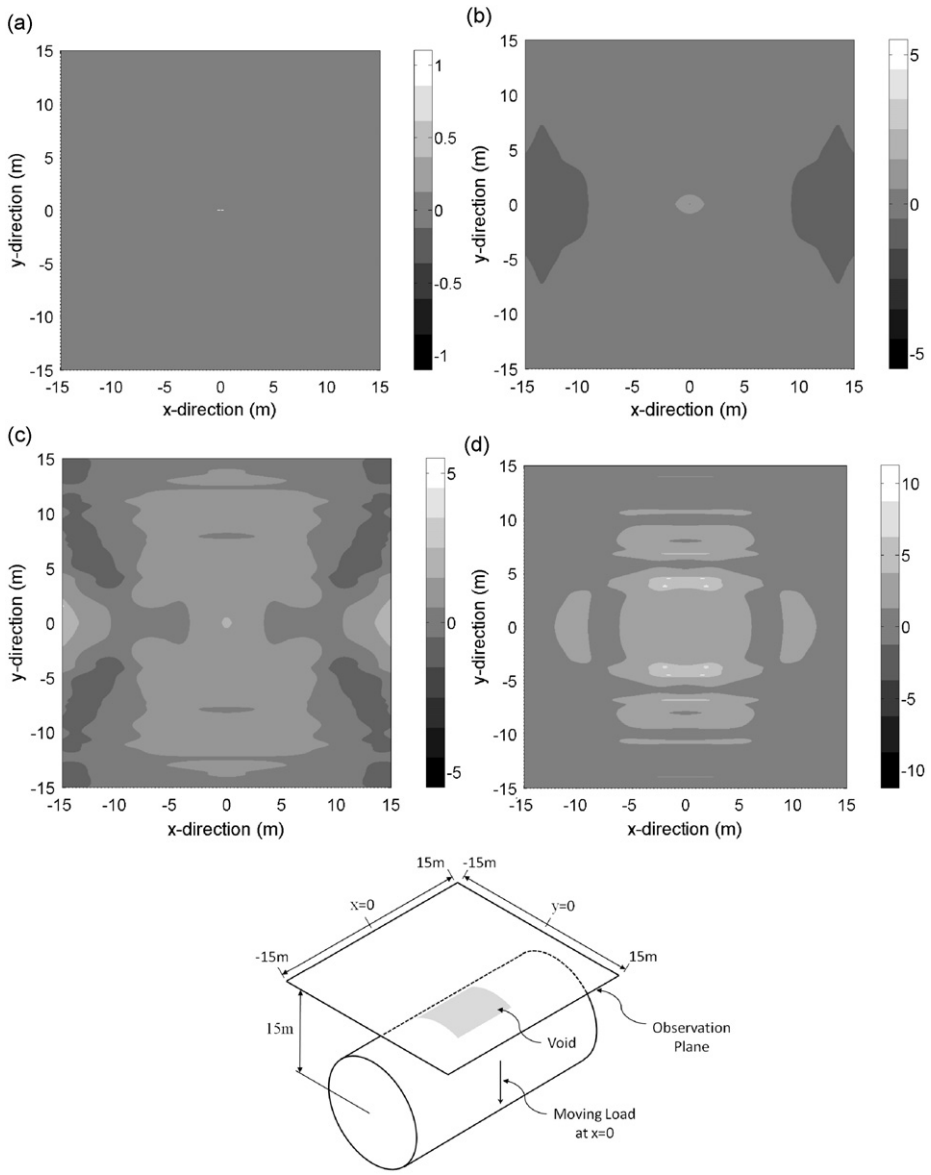

Fig. 17. Insertion gain response in dB(rms, ref 1 m/s) for case VL-1 (2 m × 67.5°) at four representative third-octave frequency passbands; moving load at $x=0$. (a) 25, (b) 50, (c) 100 and (d) 160 Hz passbands.

are compared to the PiP prediction in Fig. 12, where the difference between the two models are plotted in dB for the same four passbands; a positive difference signifies the discrete model predicts larger values than PiP.

The results from the two models show good agreement at all passbands. The maximum difference is $(+0.9, -0.7)$ dB occurring at the 25 Hz passband shown in Fig. 12(a); differences at higher frequency passbands are significantly lower (< 0.1 dB). The larger error at the low passband frequency is attributed to the truncation of the longest wavelengths by the reduced model length x_{max} = 40 m, hence the areas of greatest error occur at large x-values rather than at the center of the model. This relatively small difference between two different numerical models suggests that the discrete model is valid for a continuously coupled tunnel–soil interface. The final section considers the same tunnel–soil parameters but with the inclusion of a void.

4. Simulating voids using the discrete model

To quantify the effect of a void on vertical response compared to a continuously bonded model a number of different void configurations are investigated; Table 4 lists the void parameters. A schematic showing the tunnel, observation plane,

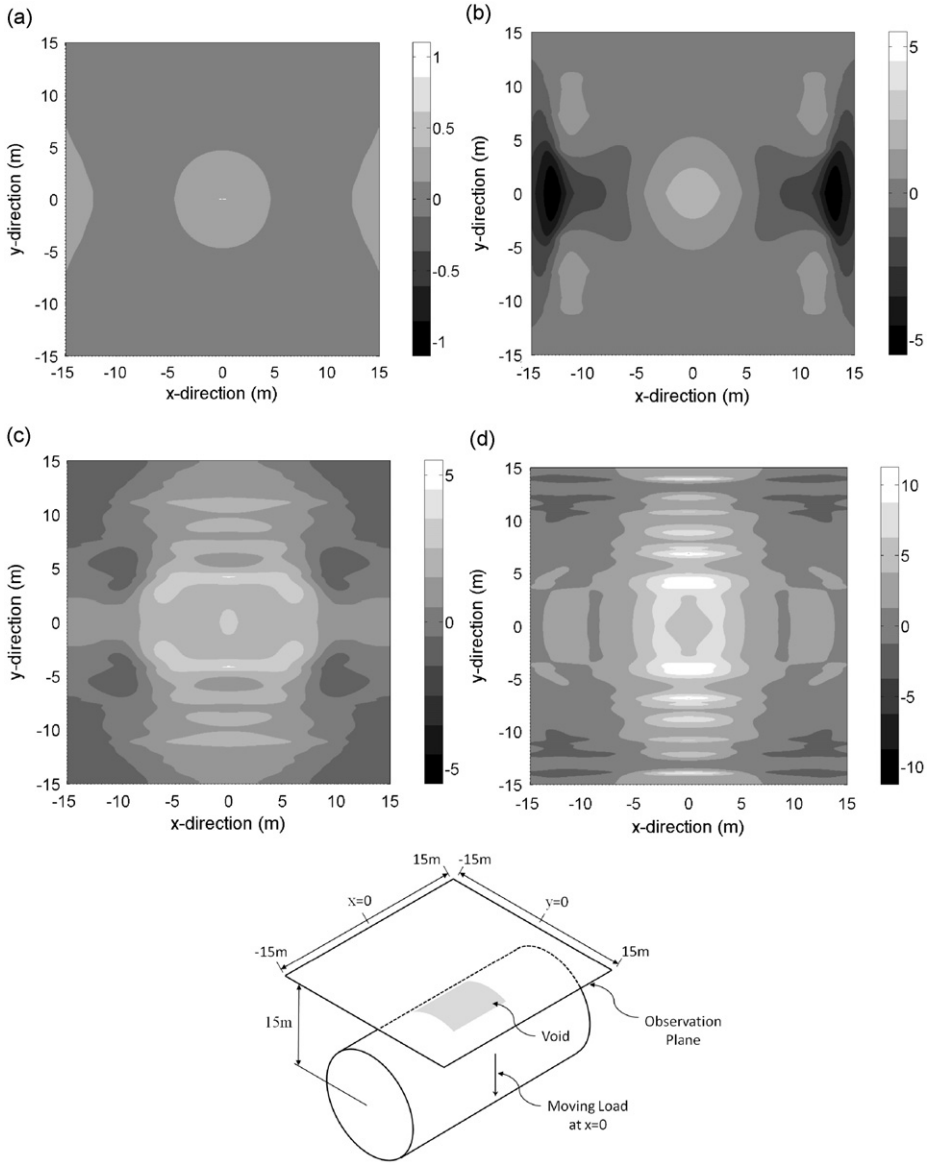

Fig. 18. Insertion gain response in dB (rms, ref 1 m/s) for case VL-2 (4 m × 67.5˚) at four representative third-octave frequency passbands; moving load at x=0. (a) 25, (b) 50, (c) 100 and (d) 160 Hz passbands.

moving load and void placement is presented in Fig. 13 with a schematic showing the void parameters in Fig. 14. For all cases the void is centered on the top of the tunnel at $(x,y) = (0,0)$ in the observation plane.

As an example of the response due to a moving load, the discrete model is used to predict the vertical particle velocity response for the case of a 4 m × 90.0° void (VA-3) subjected to a moving point-load oscillating at 100 Hz. The nine figures presented in Fig. 15 represent the response as the load position (LP) moves from left to right through the tunnel (−12 m → 12 m in 3 m intervals). When the load is relatively far from the void (LP1–LP2) the response is symmetric in both the x and y directions and seemingly unaffected by the presence of the void. As the load approaches the void location the response around the void location begins to change, as seen in the loss of x-direction symmetry developing at LP3. This void-effect remains visible through LP7 until the load is again sufficiently far away such that the void has little effect on the predicted particle velocity.

To better illustrate the effect of the void the insertion gain is calculated for the same case as shown in Fig. 16. Insertion gain is defined as the difference between the results for the void model and the continuously coupled discrete model at the same observation points and is reported in dB (rms, ref 1 m/s); a positive insertion gain signifies an increase in rms particle velocity due to the presence of a void at the tunnel–soil interface. The benefit of using the insertion gain method is seen at LP1 where a void-effect is visible even when the moving load is relatively far from the void location (compare to LP1 in

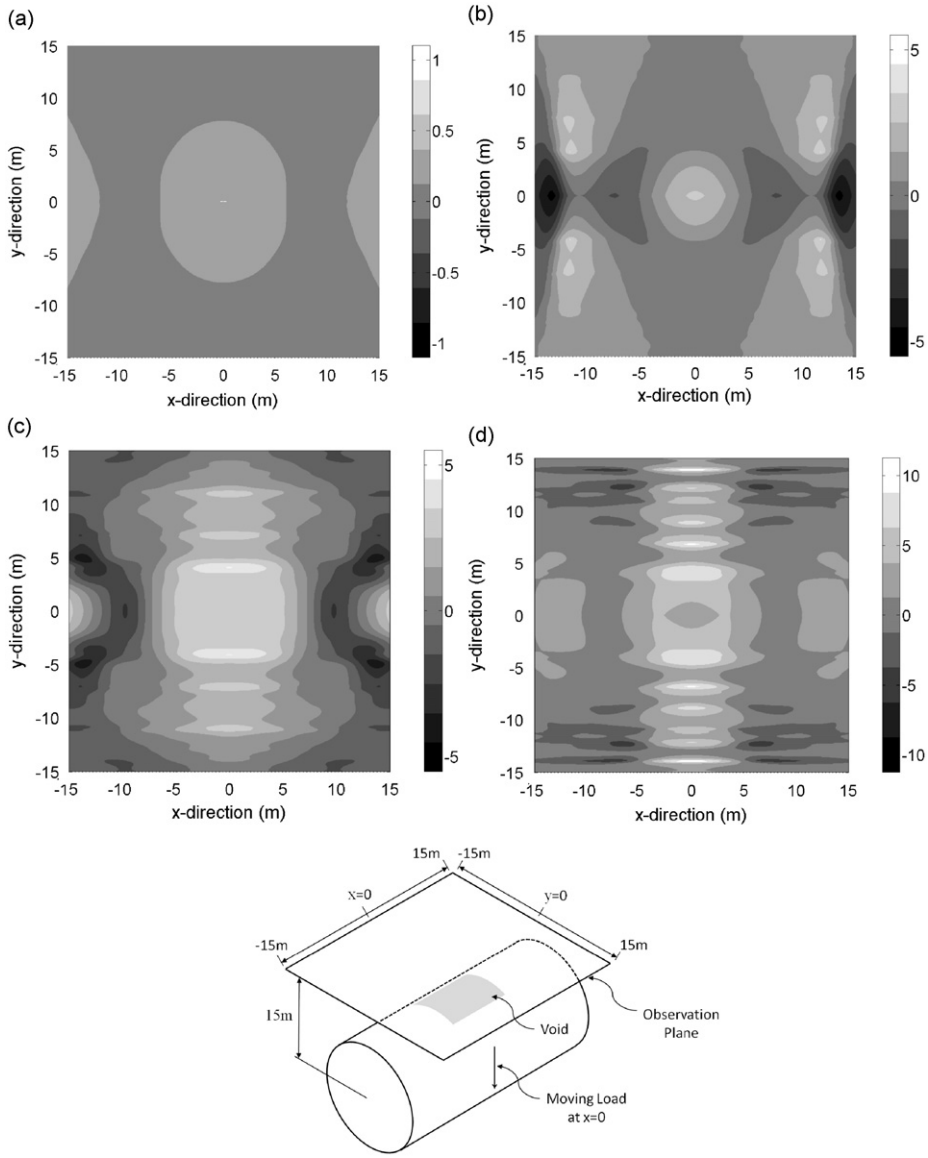

Fig. 19. Insertion gain response in dB (rms, ref 1 m/s) for case VL-3 (6 m × 67.5°) at four representative third-octave frequency passbands; moving load at x=0. (a) 25, (b) 50, (c) 100 and (d) 160 Hz passbands.

Fig. 15 where there is little evidence of disturbance due to the void). There is a distinctive "wake-effect" which causes small areas of velocity reduction by up to approximately 2.3 dB, as well as a wave energy localization behind the tunnel causing an increase of approximately 3.1 dB. The effect of the void increases as the moving load approaches the void location.

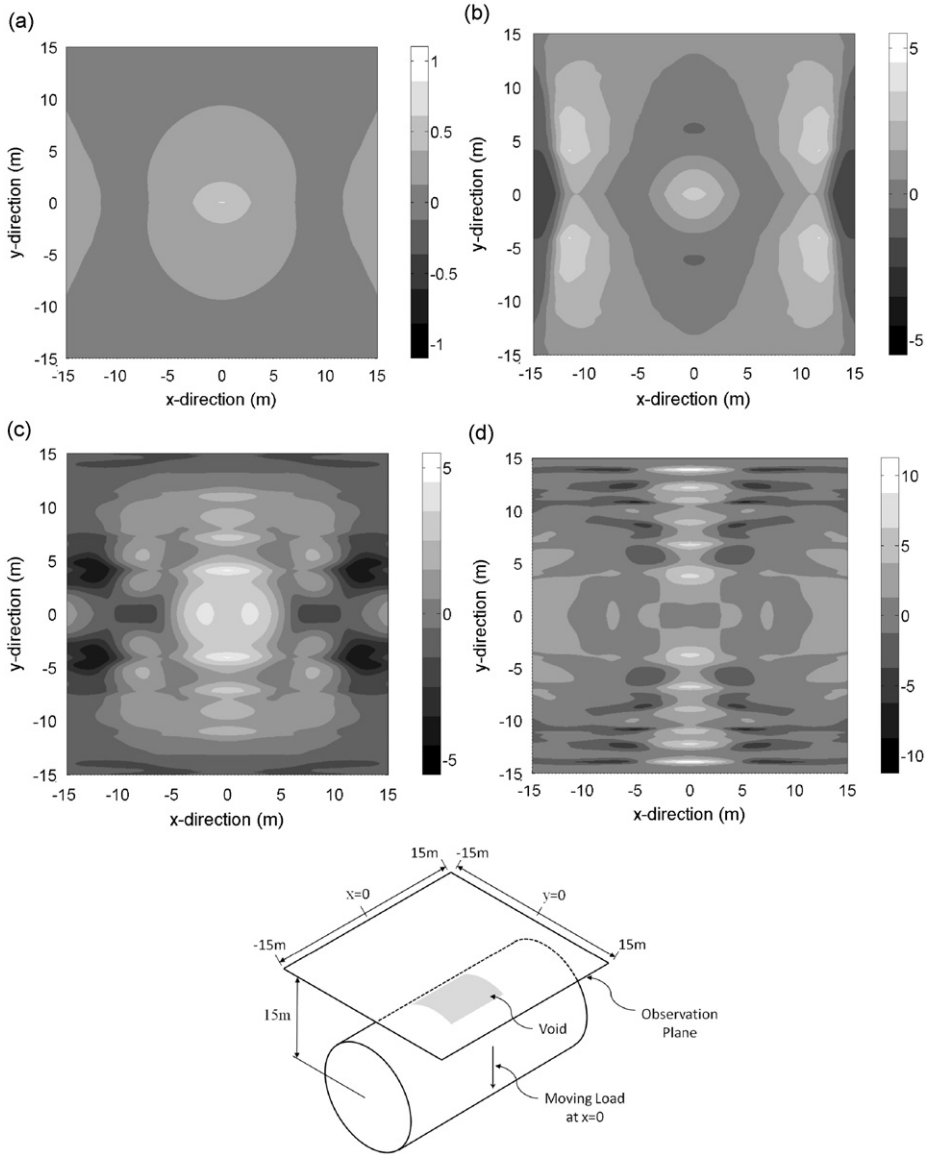

Fig. 20. Insertion gain response in dB (rms, ref 1 m/s) for case VL-4 (8 m × 67.5˚) at four representative third-octave frequency passbands; moving load at $x=0$. (a) 25, (b) 50, (c) 100 and (d) 160 Hz passbands.

Table 5
Peak vertical insertion gain (IG) for void length sensitivity study at 25, 50, 100 and 160 Hz passbands measured in dB (rms, ref 1 m/s).

Case	25 Hz	50 Hz	100 Hz	160 Hz
VL-1	(−0.0,+0.1)	(−0.3,+0.5)	(−1.3,+1.5)	(−0.9,+3.3)
VL-2	(−0.0,+0.2)	(−1.7,+2.0)	(−0.9,+2.7)	(−3.4,+8.5)
VL-3	(−0.0,+0.4)	(−2.2,+2.6)	(−1.4,+3.4)	(−5.2,+8.3)
VL-4	(−0.0,+0.4)	(−1.5,+2.8)	(−3.4,+3.9)	(−5.6,+8.1)

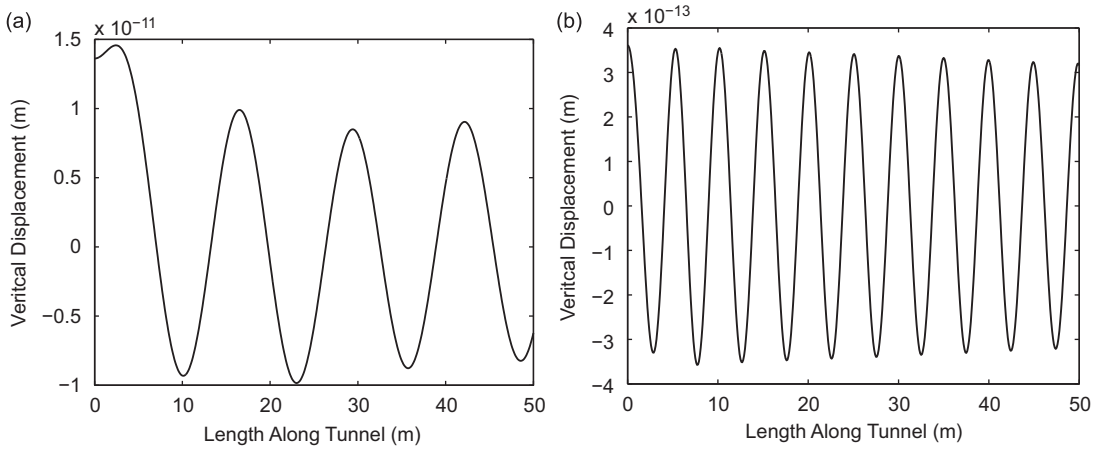

Fig. 21. Vertical response of tunnel at (a) 25 and (b) 160 Hz.

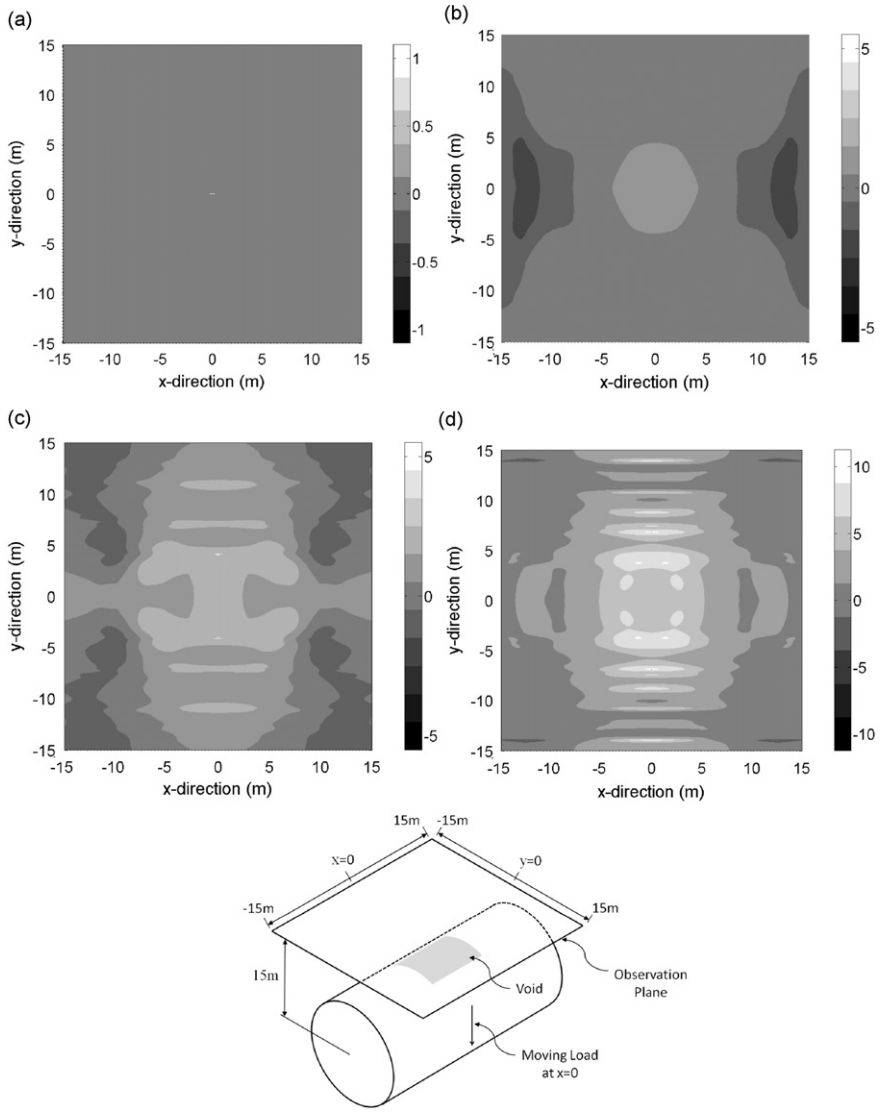

Fig. 22. Insertion gain response in dB (rms, ref 1 m/s) for case VA-1 (4 m × 45°) at four representative third-octave frequency passbands; moving load at x=0. (a) 25, (b) 50, (c) 100 and (d) 160 Hz passbands.

The average insertion gain over the observation plane reaches a maximum when the load is directly under the void (LP5) with areas of $(-3.4,+4.2)$ dB in the near-field of the void.

This case study suggests the void has a significant effect when the load is directly under the void as well as a moderate effect when the load is relatively far from the void. As the average IG value reaches a maximum when the load is directly under the void, results for the void sensitivity studies will be presented for this load location only. It should be noted that the wake-effect is present in all cases when the load is reasonably far from the void location. The results for the two sensitivity studies are presented in the following subsections: void length sensitivity and void sector angle sensitivity.

4.1. Results for void length sensitivity study

The effect of void length on vertical rms velocity response at different third-octave passbands is investigated for a 67.5° sector angle using four void lengths: 2, 4, 6 and 8 m (see Table 4). The observation plane responses are presented in Figs. 17–20.

A trend common in all passbands is the IG magnitude increases as the length of the void is increased. For example, the peak IG values at the 100 Hz passband increase from $(-1.3,+1.5)$ dB for case VL-1 to $(-3.4,+3.9)$ dB for case VL-4. Table 5

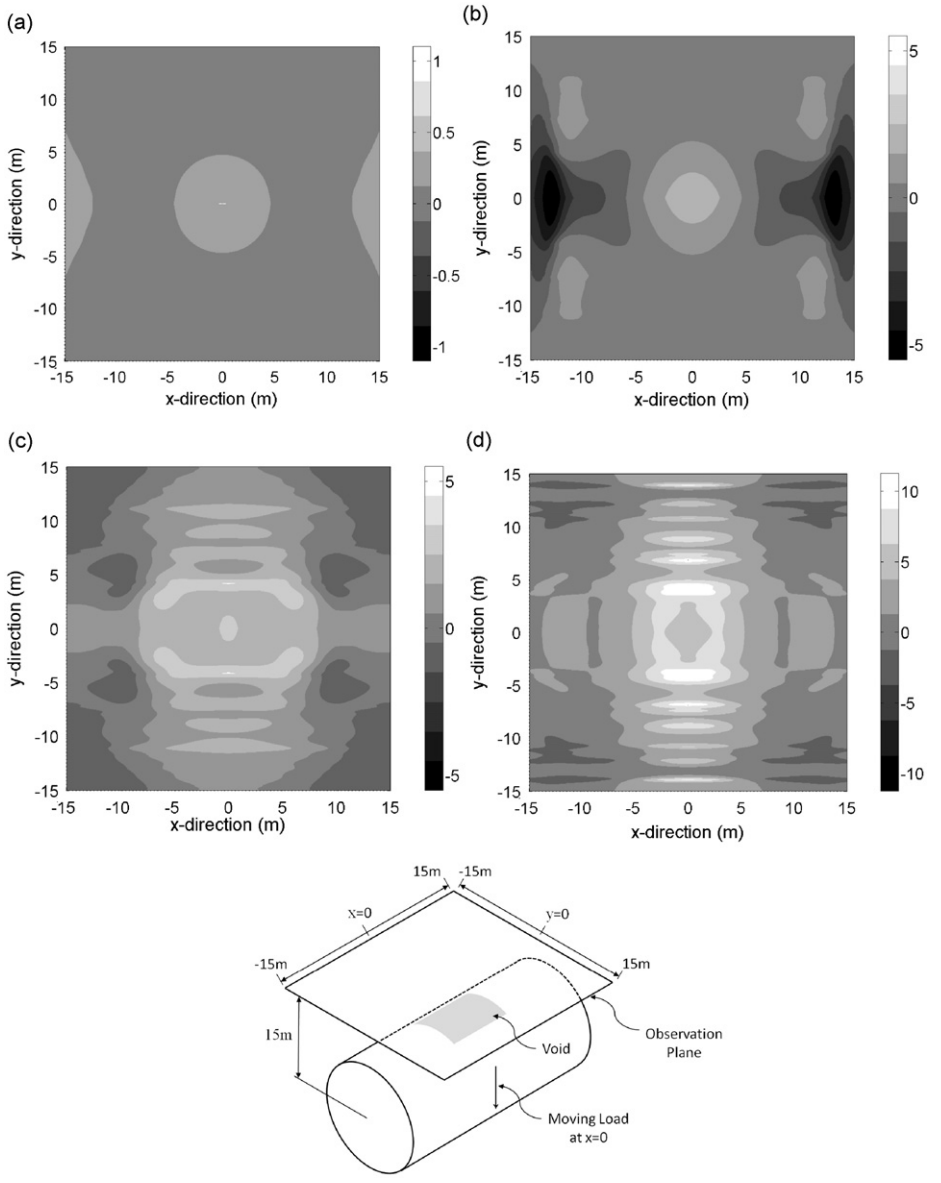

Fig. 23. Insertion gain response in dB (rms, ref 1 m/s) for case VA-2 (4 m × 67.5°) at four representative third-octave frequency passbands; moving load at $x=0$. (a) 25, (b) 50, (c) 100 and (d) 160 Hz passbands.

lists the peak insertion gains for the four cases at the passbands listed. Furthermore, the density of increased IG values increases with void length; only small areas of insertion gain with magnitude greater than 1 dB are visible in the 50 Hz passband for case VL-1 while the bulk of the observation plane has IG greater than 1 dB for case VL-4 with substantial areas of 2 dB or more.

This variation in response with void length is attributed to how the vibration energy is transformed into pressure and shear-waves when a void is present at the tunnel–soil interface. Since there is no force transmission at the void site, motion of the tunnel at this location will not directly result in wave propagation. Fig. 21 shows the vertical response of the tunnel for a void-free case at 25 and 160 Hz. The average wavelength at 25 Hz is approximately 13 m while at 160 Hz it is approximately 5 m. For case VL-1 the void is only 2 m long which is relatively small compared to the 25 Hz wavelength thus it has little effect on the response at the observation plane (Fig. 17(a)); the bulk of the wavelength bridges the void. At 160 Hz the void length is more substantial relative to the wavelength thus it has a greater effect (Fig. 17(d)); the void accounts for almost half a wavelength thus a significant amount of energy is not transmitted to the soil above the tunnel resulting in peak IG values of $(-0.9,+3.3)$ dB. The lack of force transmission at the void results in higher interface forces elsewhere around the tunnel thus energy localization in the wavefronts occurs relative to the void-free case. This explains why the void causes IG losses at some locations (no force transmission across the void) and IG increases at others (energy

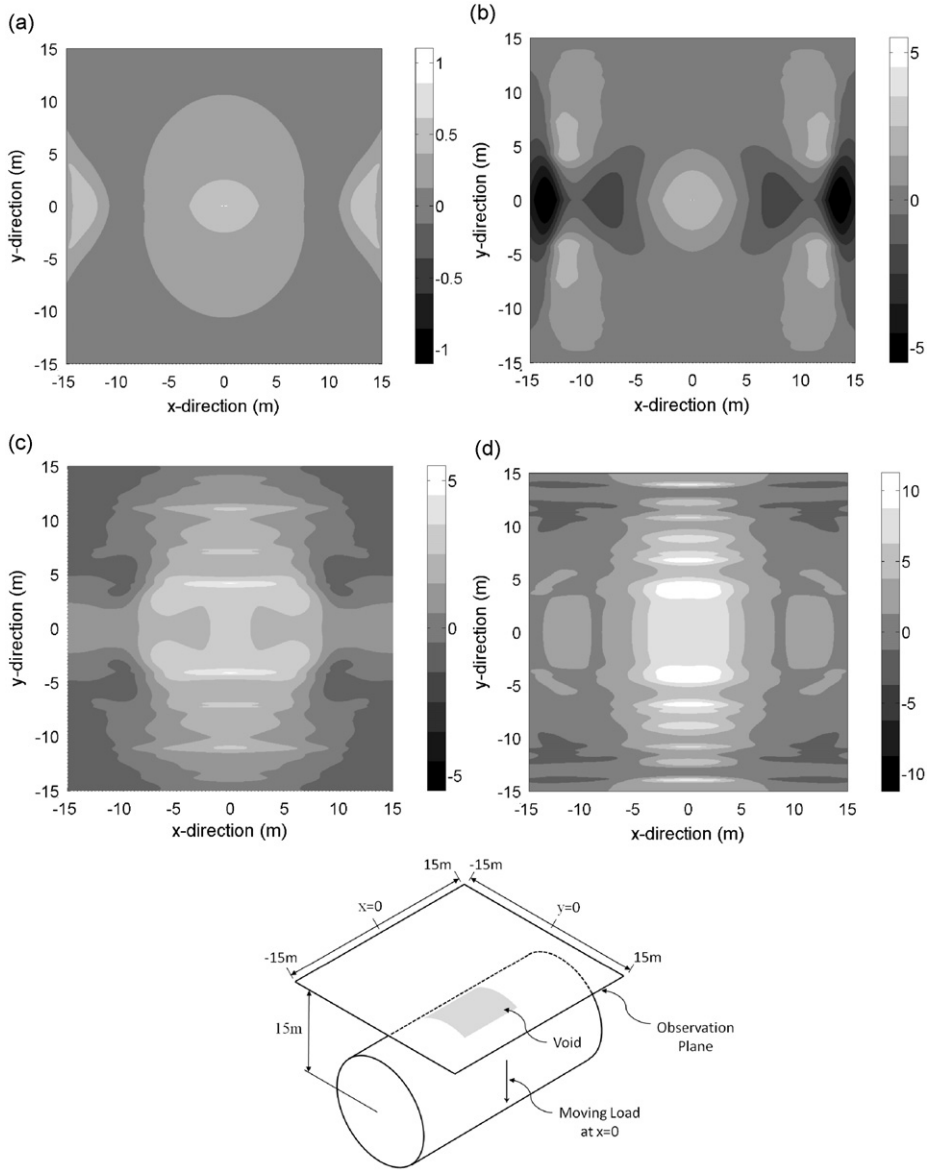

Fig. 24. Insertion gain response in dB (rms, ref 1 m/s) for case VA-3 (4 m × 90°) at four representative third-octave frequency passbands; moving load at $x=0$. (a) 25, (b) 50, (c) 100 and (d) 160 Hz passbands.

localization to other areas of the tunnel–soil interface). However, as the void length is relatively small compared to the wavelengths the effect is mainly constrained to the near-field response (i.e. the area over the void).

For case VL-4 the void length is 8 m; this is a substantial amount of the low frequency wavelength thus the insertion gain is more significant than in the VL-1 case. However, the IG is still less than 1 dB which is relatively small and within the error range of the model (see Section 4). The 8 m void is large compared to the 160 Hz wavelength thus a large amount of vibrational energy is not transmitted through the top of the tunnel–soil interface compared to the void-free case. The result is peak insertion gains of $(-5.6,+8.1)$ dB. This is a significant change compared to the void-free case. Also the effect of the void extends further into the far field of the observation plane as a significant amount of vibrational energy has to be redistributed around the tunnel–soil interface due to the length of the void.

4.2. Results for void sector angle sensitivity study

The effect of void sector angle on vertical rms velocity response at different third-octave passbands is investigated for a 4 m void length using four void sector angles: 45°, 67.5°, 90° and 112.5° (see Table 4). The observation plane responses are presented in Figs. 22–25.

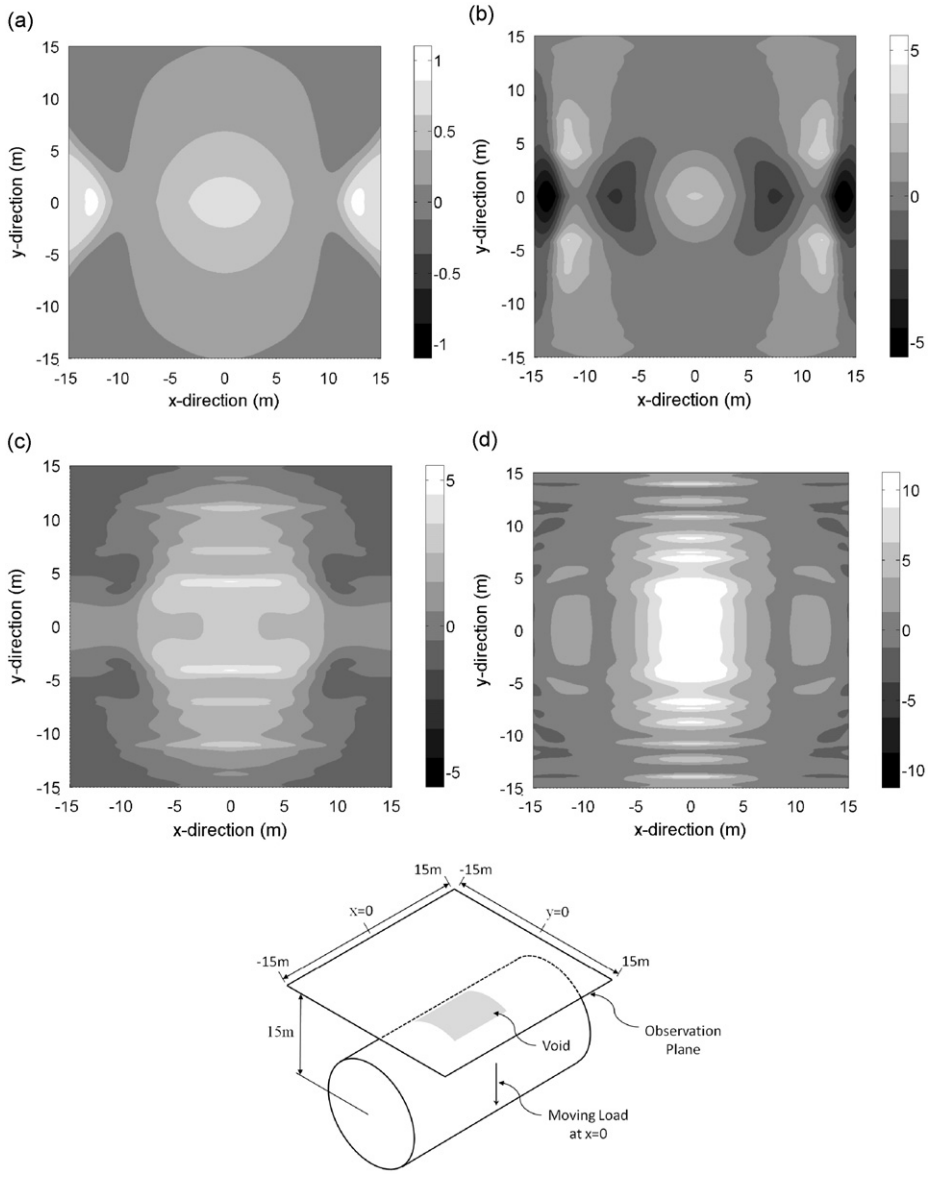

Fig. 25. Insertion gain response in dB (rms, ref 1 m/s) for case VA-4 (4 m × 112.5°) at four representative third-octave frequency passbands; moving load at x=0. (a) 25, (b) 50, (c) 100 and (d) 160 Hz passbands.

Table 6
Peak vertical insertion gain (IG) for void sector angle sensitivity study at 25, 50, 100 and 160 Hz passbands measured in dB (rms, ref 1 m/s).

Case	25 Hz	50 Hz	100 Hz	160 Hz
VA-1	(−0.0,+0.1)	(−0.6,+0.9)	(−0.7,+2.2)	(−1.9,+7.3)
VA-2	(−0.0,+0.2)	(−1.7,+2.0)	(−0.9,+2.7)	(−3.4,+8.5)
VA-3	(−0.0,+0.5)	(−2.8,+2.4)	(−1.0,+3.1)	(−3.2,+9.8)
VA-4	(−0.1,+0.9)	(−3.4,+2.6)	(−1.0,+3.4)	(−2.0,+10.9)

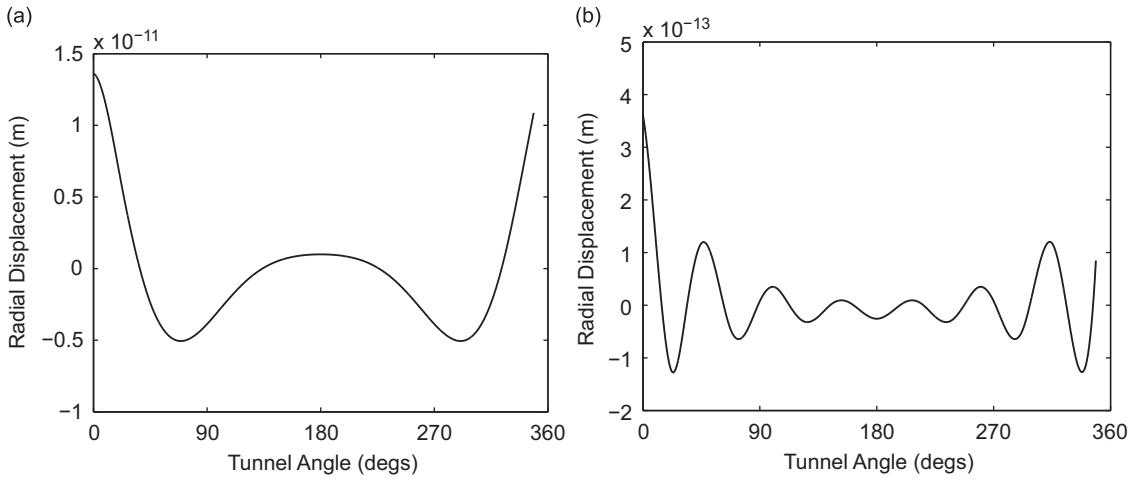

Fig. 26. Radial response of tunnel at x=0 for (a) 25 and (b) 160 Hz.

Again a common trend in all passbands is the increase in IG magnitude as the sector angle of the void is increased. For example, the peak IG values at the 100 Hz passband increase from (−0.7,+2.2) dB for case VA-1 to (−1.0,+3.4) dB for case VA-4. Table 6 lists the peak insertion gains for the four cases at the given passbands. However, unlike the void length study, the density of insertion gain over the observation plane does not largely depend on void sector angle, especially in the higher frequency passbands. The 160 Hz passband response tends to grow in magnitude as the void angle is increased (Figs. 22(d)–25(d)) while the distribution remains relatively constant.

This response is again attributed to the disruption of force transmission between the tunnel and the soil at the void location, but in the case of the void sector angle the response around the circumference of the tunnel is deemed to be the governing factor. Fig. 26 shows the radial response of the tunnel at x=0 for a void-free case at 25 and 160 Hz. The average circumferential wavelength at 25 Hz is approximately 360° while at 160 Hz it is approximately 50°.

For case VA-1 the void sector angle is 45° which is relatively small compared to the wavelength at 25 Hz. In a similar fashion to the VL-1 case, the wavelength bridges the void which essentially negates its presence. At 160 Hz the void angle is basically the same as the circumferential wavelength thus a large portion of the vibration energy is not transmitted through the top of the tunnel–soil interface resulting in significant insertion gains with peak values of (−1.9,+7.3) dB.

By case VA-4 the void sector angle is 112.5° which is a significant void for all frequency passbands. As in the void length study, the void has little effect on observation plane response for the 25 Hz passband (< 1 dB) even at this large void angle; the insertion gain at higher passbands is significant, reaching a peak of (−2.0,+10.9) dB for the 160 Hz passband.

5. Conclusions

A semi-analytical model is developed to investigate the effect of voids around an underground railway tunnel on ground vibration. The method derives the discrete transfer functions for the tunnel and soil from the Pipe-in-Pipe continuous solution. The void is simulated by uncoupling the appropriate nodes to prevent the transfer of force between the tunnel and the soil. A number of void geometries are investigated to determine how sensitive the vertical response of the soil is to changes in void size. The results from this investigation show that relatively small voids (4 m × 90°) can significantly affect the rms velocity predictions at higher frequencies (peak insertion gain: (−3.4,+8.5) dB for 160 Hz passband) while they have less effect at lower frequencies (peak insertion gain: (−1.7,+2.0) dB for 50 Hz passband). The sensitivity to void length and void sector angle was also investigated and results suggest that rms velocity predictions are sensitive to both parameters. The findings from this study suggest that the uncertainty associated with assuming a perfect bond at the tunnel–soil interface in an area with known voidage can reasonably reach ±5 dB for frequencies between 100 and 200 Hz and thus should be considered in the design process.

Acknowledgements

This work was funded in part by the Gates Cambridge Trust and the Natural Sciences and Engineering Research Council of Canada.

Appendix A

A.1. Tunnel

For displacements symmetric about $\theta=0$, $\tilde{\mathbf{H}}_{\text{tunnel}}=(a(\nu^2-1)/Eh)\tilde{\mathbf{A}}^{-1}$, where a is the mid-thickness radius of the tunnel, ν is Poisson's ratio, E is the elastic modulus, h is the thickness of the tunnel wall, and the coefficients of $\tilde{\mathbf{A}}$ are as follows:

$$a_{11}=\frac{\rho a(1-\nu^2)}{E}\omega^2-a\xi^2-\frac{(1-\nu)}{2a}n^2-\frac{1-\nu}{2a}\frac{h^2}{12a^2}n^2,\quad a_{12}=\frac{(1+\nu)}{2}\mathrm{i}\xi n$$

$$a_{13}=-\nu\mathrm{i}\xi+\frac{h^2}{12}(\mathrm{i}\xi)^3+\frac{h^2}{12a^2}\frac{(1-\nu)}{2}\mathrm{i}\xi n^2,\quad a_{21}=\frac{(1+\nu)}{2}\mathrm{i}\xi n$$

$$a_{22}=\frac{\rho a(1-\nu^2)}{E}\omega^2-\frac{a(1-\nu)}{2}\xi^2-\frac{n^2}{a}-\frac{a(1-\nu)}{2}\frac{h^2}{4a^2}\xi^2,\quad a_{23}=\frac{n}{a}+\frac{h^2}{12}\frac{(3-\nu)}{2a}\xi^2 n$$

$$a_{31}=\nu\mathrm{i}\xi-\frac{h^2}{12}(\mathrm{i}\xi)^3-\frac{h^2}{12a^2}\frac{(1-\nu)}{2}\mathrm{i}\xi n^2,\quad a_{32}=\frac{n}{a}+\frac{h^2}{12}\frac{(3-\nu)}{2a}\xi^2 n$$

$$a_{33}=\frac{\rho a(1-\nu^2)}{E}\omega^2-\frac{h^2}{12}\left(a\xi^4+\frac{2}{a}\xi^2n^2+\frac{n^4}{a^3}\right)-\frac{1}{a}+\frac{h^2}{6a^3}n^2-\frac{h^2}{12a^3}$$

where ρ is density, ω is forcing frequency, ξ is wavenumber, and n is ring-mode. For anti-symmetric displacements about $\theta=0$, a_{12}, a_{21}, a_{23} and a_{32} must be multiplied by -1.

A.2. Soil

For displacements symmetric about $\theta=0$, $\tilde{\mathbf{H}}_{\text{soil}}=\tilde{\mathbf{U}}_{\infty_{r=a}}\tilde{\mathbf{T}}^{-1}_{\infty_{r=a}}$, where the coefficients are as follows:

$$t_{11}=2\mu\mathrm{i}\xi\left(\alpha K_{n+1}(\alpha r)-\frac{n}{r}K_n(\alpha r)\right),\quad t_{12}=\mu\left((\xi^2+\beta^2)K_{n+1}(\beta r)-\frac{n}{r}\beta K_n(\beta r)\right)$$

$$t_{13}=-\mu\mathrm{i}\xi\frac{n}{r}K_n(\beta r),\quad t_{21}=2\mu\left(\frac{(n^2-n)}{r^2}K_n(\alpha r)-\frac{n}{r}\alpha K_{n+1}(\alpha r)\right)$$

$$t_{22}=\mu\mathrm{i}\xi\left(\beta K_n(\beta r)+2\frac{(n+1)}{r}K_{n+1}(\beta r)\right),\quad t_{23}=\left(2\mu\frac{(n^2-n)}{r^2}+\mu\beta^2\right)K_n(\beta r)+2\mu\frac{\beta}{r}K_{n+1}(\beta r)$$

$$t_{31}=\left(2\mu\frac{(n^2-n)}{r^2}-\lambda\xi^2+(\lambda+2\mu)\alpha^2\right)K_n(\alpha r)+2\mu\frac{\alpha}{r}K_{n+1}(\alpha r)$$

$$t_{32}=-2\mu\mathrm{i}\xi\left(\beta K_n(\beta r)+\frac{(n+1)}{r}K_{n+1}(\beta r)\right)$$

$$t_{33}=2\mu\left(\frac{(n^2-n)}{r^2}K_n(\beta r)-\frac{n}{r}\beta K_{n+1}(\beta r)\right)$$

$$u_{11}=\mathrm{i}\xi K_n(\alpha r),\quad u_{12}=\beta K_n(\beta r),\quad u_{13}=0$$

$$u_{21}=-\frac{n}{r}K_n(\alpha r),\quad u_{22}=\mathrm{i}\xi K_{n+1}(\beta r),\quad u_{23}=-\frac{n}{r}K_n(\beta r)+\beta K_{n+1}(\beta r)$$

$$u_{31}=-\frac{n}{r}K_n(\alpha r)+\alpha K_{n+1}(\alpha r),\quad u_{32}=-\mathrm{i}\xi K_{n+1}(\beta r),\quad u_{33}=-\frac{n}{r}K_n(\beta r)$$

where K is the modified Bessel function of the second kind, c_1 is pressure-wave speed, c_2 is shear-wave speed, λ is the shear modulus, $\alpha^2=\xi^2-\omega^2/c_1^2$, and $\beta^2=\xi^2-\omega^2/c_2^2$. For anti-symmetric displacements about $\theta=0$, coefficients 12, 13, 21, 32 and 33 of $\tilde{\mathbf{U}}_\infty$ and $\tilde{\mathbf{T}}_\infty$ must be multiplied by -1.

References

[1] British Standards Institution, Guide to evaluation of human exposure to vibration in buildings (1–80 Hz); BS 6472:1992.
[2] R. Hildebrand, Countermeasures against railway ground and track vibration, Report at Department of Vehicle Engineering, Stockholm, 2001.
[3] B. Griefahn, A. Marks, S. Robens, Noise emitted from road, rail and air traffic and their effects on sleep, *Journal of Sound and Vibration* 295 (2006) 129–140.
[4] T. Schultz, Synthesis of social surveys on noise annoyance, *Journal of the Acoustical Society of America* 64 (1978) 377–405.
[5] K. Kryter, Community annoyance from aircraft and ground vehicle noise, *Journal of the Acoustical Society of America* 72 (1982) 1212–1242.
[6] S. Fidell, D. Barber, T. Schultz, Updating a dosage-effect relationship for the prevalence of annoyance due to general transportation noise, *Journal of the Acoustical Society of America* 89 (1991) 221–233.
[7] H. Miedema, H. Vos, Exposure-response relationships for transportation noise, *Journal of the Acoustical Society of America* 104 (6) (1998) 3432–3445.
[8] British Standards Institution, Mechanical vibration—ground-borne noise and vibration arising from rail systems—part 1: general guidance; BS ISO 14837-1:2005.
[9] C. Jones, J. Block, Prediction of ground vibration from freight trains, *Journal of Sound and Vibration* 193 (1) (1996) 205–213.
[10] P. Grootenhuis, Floating track slab isolation for railways, *Journal of Sound and Vibration* 51 (3) (1977) 443–448.
[11] R. Greer, C. Manning, Vibration isolation for railways, *Acoustics Bulletin* 23 (3) (1998) 13–17.
[12] X. Sheng, C. Jones, D. Thompson, A comparison of a theoretical model for quasi-statically and dynamically induced environmental vibration from trains with measurements, *Journal of Sound and Vibration* 267 (3) (2003) 621–635.
[13] J. Forrest, Modelling of Ground Vibration from Underground Railways, PhD Thesis, University of Cambridge, UK, 1999.
[14] K. Chua, K. Lo, T. Balendra, Building response due to subway train traffic, *Journal of Geotechnical Engineering, Proceedings of the ASCE* 121 (11) (1995) 747–754.
[15] C. Jones, D. Thompson, M. Petyt, A model for ground vibration from railway tunnels, *Transport* 153 (2) (2002) 121–129.
[16] M. Mohammadi, D. Karabalis, Dynamic 3D soil-railway track interaction by BEM-FEM, *Earthquake Engineering and Structural Dynamics* 24 (9) (1995) 1177–1193.
[17] A. Stamos, D. Beskos, Dynamic analysis of large 3D underground structures by the BEM, *Earthquake Engineering and Structural Dynamics* 24 (6) (1995) 917–934.
[18] A. Stamos, D. Beskos, 3D seismic response analysis of long lined tunnels in half-space, *Soil Dynamics and Earthquake Engineering* 15 (1996) 111–118.
[19] L. Andersen, C. Jones, Coupled boundary and finite element analysis of vibration from railway tunnels—a comparison of two- and three-dimensional models, *Journal of Sound and Vibration* 293 (3–5) (2006) 611–625.
[20] X. Sheng, C. Jones, D. Thompson, Ground vibration generated by a harmonic load moving in a circular tunnel in a layered ground, *Proceedings of the 10th International Meeting on low Frequency Noise and Vibration and its Control*, 2002, pp. 161–176.
[21] X. Sheng, C. Jones, D. Thompson, Prediction of ground vibration from trains using the wavenumber finite and boundary element methods, *Journal of Sound and Vibration* 293 (3-5) (2006) 575–586.
[22] X. Sheng, C. Jones, D. Thompson, Modelling ground vibration from railways using wavenumber finite- and boundary-element methods, *Proceedings of the Royal Society A* 461 (2005) 2043–2070.
[23] D. Clouteau, M. Arnst, T. Al-Hussaini, G. Degrande, Freefield vibrations due to dynamic loading on a tunnel embedded in a stratified medium, *Journal of Sound and Vibration* 283 (2005) 173–199.
[24] G. Degrande, D. Clouteau, R. Othman, M. Arnst, H. Chebli, R. Klein, P. Chatterjee, B. Janssesns, A numerical model for ground-borne vibrations from underground railway traffic based on a periodic finite element—boundary element formulation, *Journal of Sound and Vibration* 293 (2006) 645–666.
[25] S. Gupta, W.F. Liu, G. Degrande, G. Lombaert, W.N. Liu, Prediction of vibrations induced by underground railway traffic in Beijing, *Journal of Sound and Vibration* 310 (2008) 608–630.
[26] S. Gupta, Y. Stanus, G. Lombaert, G. Degrande, Influence of tunnel and soil parameters on vibration from underground railways, *Journal of Sound and Vibration* 327 (1-2) (2009) 70–91.
[27] J. Forrest, H. Hunt, A three-dimensional model for calculating of train-induced ground vibrations, *Journal of Sound and Vibration* 294 (4–5) (2006) 678–705.
[28] J. Forrest, H. Hunt, Ground vibration generated by trains in underground tunnels, *Journal of Sound and Vibration* 294 (4–5) (2006) 706–736.
[29] S. Gupta, M. Hussein, G. Degrande, H. Hunt, Clouteau, A comparison of two numerical models for the prediction of vibrations from underground railway traffic, *Soil Dynamics and Earthquake Engineering* 27 (7) (2007) 608–624.
[30] M. Hussein, Vibration from Underground Railways. PhD Thesis, University of Cambridge, UK, 2004.
[31] M. Hussein, H. Hunt, A numerical model for calculating vibration from a railway tunnel embedded in a full-space, *Journal of Sound and Vibration* 305 (3) (2007) 401–431.
[32] M. Hussein, H. Hunt, A numerical model for calculating vibration due to a harmonic moving load on a floating-slab track with discontinuous slabs in an underground railway tunnel, *Journal of Sound and Vibration* 321 (2009) 363–374.
[33] K. Komiya, K. Takiyama, H. Akagi, Settlement behaviour of a shield tunnel constructed in subsiding reclaimed area, *Proceedings of Geotechnical Aspects of Underground Construction in Soft Ground*, 2006.
[34] Tunnel vision—the future role of tunnels in transport infrastructure, Parliamentary Office of Science and Technology, 90, 1997.
[35] G. Rennie, Monitoring Earth's subsurface from space, *Science and Technology Review* (April) (2005) 4–11.
[36] D. Newland, *An Introduction to Random Vibrations Spectral and Wavelet Analysis*, third ed., Longman, Harlow, Essex, England, 1993.
[37] R. Langley, On quasi-stationary approximations to non-stationary random vibration, *Journal of Sound and Vibration* 113 (2) (1987) 365–375.
[38] F. Frederich, Effect of track geometry on vehicle performance, *Zeitschrift für eisenbahnwesen und vekehrstechnik Glasers auualen* 108 (12) (1984) 355–362.